Peer reviewed version

University of Bristol - Explore Bristol Research
General rights

CORROSION OF THE ALLOYS MAGNOX AL80, MAGNOX ZR55 AND PURE MAGNESIUM IN AIR CONTAINING WATER VAPOUR

Keith R Hallam[a,*], Peter C Minshall[b], Peter J Heard[c], Peter EJ Flewitt[a,d]

[a]University of Bristol
Interface Analysis Centre
School of Physics
HH Wills Physics Laboratory
Tyndall Avenue
Bristol BS8 1TL
United Kingdom
k.r.hallam@bristol.ac.uk

[b]Magnox Limited
Oldbury Technical Centre
Oldbury Naite
Thornbury
South Gloucestershire BS35 1RQ
United Kingdom
peter.c.minshall@magnoxsites.com

[a]University of Bristol
Interface Analysis Centre
School of Physics
HH Wills Physics Laboratory
Tyndall Avenue
Bristol BS8 1TL
United Kingdom
peter.heard@bristol.ac.uk

[d]University of Bristol
School of Physics
HH Wills Physics Laboratory
Tyndall Avenue
Bristol BS8 1TL
United Kingdom
peter.flewitt@bristol.ac.uk

[*]Corresponding author

ABSTRACT

Understanding the corrosion susceptibility of Magnox alloys during short- and long-term storage in moist air is important. Corrosion of Magnox AL80, Magnox ZR55 and magnesium has been studied in air containing water partial pressures between 200 vppm and ~80000 vppm, at temperatures of 46 °C to 96 °C. Specimens were exposed to air, with and without CO_2, and argon gas. Metal consumption rates were measured and corrosion products characterised, using scanning electron and optical microscopy, energy dispersive x-ray microanalysis, x-ray diffraction and secondary ion mass spectrometry. Results show the importance of CO_2 gas for suppressing breakaway corrosion in moist air.

1   INTRODUCTION

Of the fleet of UK gas-cooled Magnox-type nuclear power stations that were designed, constructed and commissioned during the 1950s and 1960s, the last ceased generating electricity at the end of 2015 [1]. All the other reactors, most of which achieved a 40-year operating life, are now in various stages of

decommissioning. The fuel elements in these first generation gas-cooled, graphite-moderated nuclear reactors consist of metallic uranium rods within sealed cans of Magnox AL80 alloy. This alloy is magnesium-based, nominally containing 0.80 wt% aluminium together with 50 ppm by weight beryllium. This alloy normally undergoes negligible corrosion in the dry carbon dioxide (CO_2) gas used to cool the reactors at power. During reactor operation, the fuel cans achieve temperatures within the range 250 °C to 450 °C [2]. There are, however, occasions where Magnox alloy fuel elements are exposed to air. These include outages for maintenance, sometimes quite prolonged, and, most significantly, during defueling following the final shutdown of the reactor. In these circumstances, the temperature of the Magnox alloy cans is, at most, about 100 °C and the water vapour partial pressure is that of the ambient air outside the reactor, about 2000 Pa to 3000 Pa.

To underwrite the safe storage of fuel in the shutdown condition, it is necessary to have an understanding of the extent and rate of corrosion of the Magnox alloy cans in moist air. In particular, it is essential to know whether the resulting corrosion product is protective. If it is, then the extent of corrosion can be neglected; if it is not, and the corrosion obeys a linear rate law; a significant quantity of corrosion product can be formed. During decommissioning, if the corrosion leads to penetration of a Magnox alloy can then the irradiated fuel will be exposed, with consequential safety implications. There are no data available that consider the corrosion of Magnox AL80 under these shutdown conditions. Friskney [3] has published data on the reaction in dry steam at a pressure of ~10^5 Pa in the temperature range 100 °C to 300 °C. Parsons and Friskney [4] measured corrosion rates in moist argon gas where the minimum water vapour pressure was about 125000 Pa and the minimum temperature was 85 °C. It was apparent from their results that there was a change in the corrosion mechanism at a relative humidity of about 0.3 and thus it would be hard to justify extrapolation of the existing data beyond the experimental range. There are, however, published studies on the corrosion of pure magnesium, and magnesium alloys such as AZ31, in conditions that are relevant to shutdown Magnox-type reactors in air [5-11]. These suggest that in moist air, at room temperature, the kinetics of magnesium corrosion are described by an inverse logarithmic expression, leading to the formation of a protective surface layer. At higher temperatures and humidity, the growth rate of corrosion product is linear with time and is, therefore, not protective. In addition, there is evidence that the presence of small concentrations of aluminium (2.5 wt% to 3.5 wt%) reduces the corrosion rate compared with that for pure magnesium [9,10]. It should be recognised that the aluminium content of the AZ alloys is higher than that of Magnox AL80 and, in addition, the AZ alloys also contain zinc (0.7 wt% to 1.3 wt%) [8].

Unfortunately, the extant data on Magnox alloy and pure magnesium corrosion is not sufficient to determine the expected behaviour of Magnox AL80 during prolonged storage in air where clad temperatures lie in the range of about 20 °C to 80 °C and water vapour concentrations will be, at a maximum, that of ambient air, i.e. no more than 30000 vppm at temperatures at, or a little above, ambient. During extended storage, the reactor atmospheres may be dried and water vapour concentrations will be lower. No data for Magnox alloy corrosion are available in these conditions of temperature and water vapour pressure, and there are virtually no data for the corrosion of pure magnesium in this range. The only relevant data obtained previously by the CEGB were at water vapour pressures in excess of 125000 vppm and temperatures above 100 °C [4] and are inappropriate to assess corrosion rates.

The experimental measurements made by Parsons and Friskney [4] show the bulk corrosion reaction to be:

$$Mg + 2H_2O \rightarrow Mg(OH)_2 + H_2 \tag{1}$$

and that, for the majority of conditions, the kinetics are linear with time, after an induction period of up to a few hours. Some measurements at higher temperatures showed rates that decreased with time, characteristic of parabolic or logarithmic kinetics. The measurements showed a discontinuity in the variation of corrosion rate with relative humidity at a value of about 0.15. Above this value, the corrosion rates showed a clear dependency on temperature; below a relative humidity of 0.15, the rates were effectively independent of temperature

This paper describes laboratory tests undertaken to simulate the decommissioning and storage conditions for air containing minor concentrations of CO_2 and with CO_2 removed. Some specimens of pure magnesium metal were included in the experiments to enable comparisons to be made with studies reported in the literature [5-8,10]. In addition, specimens of the two-phase magnesium alloy Magnox ZR55, containing zirconium in the range 0.45 wt% to 0.65 wt%, were included. This latter alloy has a higher creep resistance than Magnox AL80 and was employed in the manufacture of the so-called splitter blades used to strengthen some Magnox alloy fuel elements against distortion during in-reactor service. The splitters were removed prior to despatch of the fuel for reprocessing and stored in concrete vaults at the power stations. The results are discussed by comparison with the results of previous workers and with respect to the mechanisms controlling corrosion of Magnox alloy fuel elements during decommissioning and storage. Finally, conclusions are presented.

2 MATERIALS AND METHODS

2.1 Background

The experiments undertaken by Parsons and Friskney [4] at water vapour pressures of less than one atmosphere were carried out in flowing gas, the specimens being periodically withdrawn for weighing. The measurements were made within sealed autoclaves to which known masses of water had been added. For the proposed experiments the anticipated rates would be slow enough that mass transfer and heat transfer effects on the corrosion could be neglected and the choice of static against flowing measurements was a matter of experimental convenience. Laboratory borosilicate glass was used and apparatus was designed to avoid contact between glass and specimen surfaces. The majority of the specimens investigated were to be the alloy Magnox AL80, used for cladding of the fuel elements. However, results from pure magnesium would enable comparison with a wider body of literature data. In addition, specimens of the alloy Magnox ZR55, used for the splitter blades of Magnox fuel elements, were included. The geometry of the specimens used in the experiments were discs of mass ~0.6 g, 17 mm diameter and 1.5 mm thick.

2.2 Materials

2.2.1 Magnox AL80

A Magnox AL80 alloy (see Table 1 for composition) extrusion supplied by Magnox Limited provided the source material for the manufacture of test specimen discs. The full-size extrusion was first machined (Fishponds Precision Engineering Limited, Bristol, United Kingdom) to generate four strips of uneven thickness. These strips were then shortened in length and hot-rolled using a facility at the Department of Materials, University of Sheffield, United Kingdom. A step-wise approach to hot-rolling the strips to the desired thickness was adopted. Starting with strips up to 15 mm thick, at the root of the fin, material was first given a 20 min soak at 500 °C under argon gas. Strips were then successively rolled to 12 mm, 10 mm,

8 mm, 6 mm, 3 mm and 1.5 mm with 10 min soaks, again at 500 °C under argon, between each rolling step. Because of the non-uniform thickness of the starting material, rolling caused strips to become curved and it was necessary at stages to reduce the length to complete the rolling. At the end of the rolling process, the materials was given a final 2hr soak under argon at 515 °C before being oil-quenched.

After this processing route, the specimens used in the tests were ultimately discs ~17 mm in diameter and ~1.5 mm thick water-jet cut from the hot-rolled Magnox AL80. This ensured minimal mechanical damage at the edges of the specimens. Each of these was approximately 0.6 g in mass and had a nominal surface area of 5.34×10^{-4} m^2 after a 3 mm diameter hole was drilled to allow suspension inside the corrosion reaction vessels. Before testing, each specimen, with an as-rolled surface finish, was degreased by ultrasonic cleaning in acetone, etched for a minimum of five minutes in 2 % $^w/_v$ citric acid at room temperature using an ultrasonic bath, washed in deionised water, rinsed with methanol, dried and weighed. At intervals during reaction and after completion of experiments, the specimens were reweighed before selection for optical microscopy, scanning electron microscopy and/or x-ray diffraction (XRD).

2.2.2 Magnox ZR55

Wrought feed stock material for the manufacture of Magnox ZR55 splitters was produced from cast cylindrical billets by extrusion. The splitter material is heat treated to produce grain sizes in the range of 0.25 mm to 0.75 mm. Splitter blades were produced by machining extruded strip. The specimens used in the tests reported on here were discs ~17 mm in diameter and ~1.9 mm thick water-jet cut from as-supplied Magnox ZR55 splitter material (see Table 1 for composition). Each was ~0.7 g in mass and had a nominal surface area of 5.59×10^{-4} m^2 after a 3 mm diameter hole was drilled to allow suspension inside the reaction vessels. With no prior changes made to the as-supplied surface finish, the discs were degreased by ultrasonic cleaning in acetone, etched for a minimum of five minutes in 2 % $^w/_v$ citric acid at room temperature using an ultrasonic bath, washed in deionised water, rinsed with methanol, dried and weighed. At intervals during corrosion testing and after completion of experiments, the specimens were reweighed before selection for optical microscopy, scanning electron microscopy and/or XRD.

2.2.3 Pure magnesium

The specimens used in the tests were 99.9 % purity magnesium discs 15.0 mm in diameter and 1.0 mm thick purchased from Goodfellow Metals (part number MG000340 099-538-597; see Table 1 for composition), supplied in an as-rolled condition. These were approximately 0.3 g in mass and each had a nominal surface area of 3.96×10^{-4} m^2 after a 3 mm diameter hole was drilled in each to allow suspension inside the corrosion reaction vessels. Starting from the as-received condition, the same preparation and evaluation procedures described for the Magnox AL80 and ZR55 were then adopted.

2.3 Corrosion test procedure

Figure 1 presents a schematic diagram of the overall corrosion experiment rig where natural compressed air (i.e. not an artificial mixture of N_2, O_2, etc.) containing <30 ppm H_2O was used for the majority of the experiments described here. A sodium hydroxide (NaOH) scrubber and citric acid ($C_6H_8O_7$) neutraliser arrangement was available to generate a CO_2-free air supply when needed. In a number of experiments argon gas was used to provide both an H_2O-free and CO_2-free initial gas phase. Distilled water was used in the rig bubblers, with the majority of experiments targeting high relative humidities during the 'dynamic' experiments, where air or argon was flowing through the rigs. Bypass lines could be used to divert a

proportion of the incoming gas streams around the bubblers to allow adjustment of the resulting water vapour pressure. The bubblers could operate either at room temperature or be heated, in which case water temperatures of 60 °C were typically adopted. The gas lines between the bubblers and reaction vessels could be heated using wrap tapes to maintain elevated gas phase temperatures and, thus, ensure high humidity gas was fed to the reaction vessels. Silica wool lagging was wrapped around bubblers, gas lines and reaction vessels to maximise temperature uniformity. Temperature and relative humidity sensors were installed in the reaction vessel gas supply lines. Temperature sensors were placed into the water bubblers and reaction vessels. Data from all sensors were logged by computer every ten seconds throughout the exposure experiments. In all cases, specimens were suspended via their pre-drilled 3mm diameter holes from notched PTFE 'branches' of an AISI 316 stainless steel 'trunk' arrangement linked to the top of the glass reaction vessels. This allowed the various metals and alloys to be distributed throughout the reaction vessel volume without any direct metal-metal contact, which might otherwise have risked the creation of electrolytic corrosion sites.

In a series of 'static' experiments, 'buckets' held in place within the sealed reaction vessels supplied a fixed volume of distilled water, of an amount (0.100 mL) designed to generate 0.125 atm of H_2O within the 1 L reaction vessels. Silica gel was used to dry the incoming gas so that the only moisture available was that pre-introduced into the reaction vessel bucket. Gases were passed through the vessels to flush them before they were sealed and the temperatures raised. Separate experiments were performed at 90 °C gas temperature using either high-purity argon as the base gas or dry, CO_2-free air.

Using this rig, experiments were performed that could be characterised as follows:

- Moist air containing CO_2, flowing
- Moist air containing CO_2, static
- Moist air without CO_2, flowing
- Dry air without CO_2, static
- Moist argon without CO_2, flowing
- Dry argon without CO_2, static.

Finally, one example specimen of each of the three materials - Magnox AL80, Magnox ZR55 and pure magnesium - was suspended on a PTFE branch above a borosilicate beaker in the open laboratory under ambient conditions of temperature and humidity. These specimens were periodically weighed for comparison with specimens exposed in the reaction vessels.

2.4   Methods

2.4.1   Weighing

A Sartorius Genius self-calibrating electronic balance with 0.0001 g accuracy was used to determine the mass of all specimens before and after exposure.

2.4.2   Scanning electron microscopy

To identify the surface morphology of the specimens, imaging was performed in a Jeol JSM6100 scanning electron microscope (SEM) fitted with a tungsten filament electron source. Imaging at a series of magnifications was undertaken using the secondary electron mode and an incident beam energy of 20 keV.

2.4.3   X-ray diffraction

To characterise the test specimens, a Philips Xpert Pro diffractometer with a CuKα radiation source (λ = 1.5406 Å) was used (generator voltage of 40keV; tube emission current of 30 mA) to acquire spectra between 2θ of 5 ° and 120 °, with a step size of 0.02 ° and a 1 s dwell time. Phase identification was then performed using the ICDD (formerly JCPDS) spectral library and standard curve fitting software.

2.4.4 Focused ion beam

A combined focused ion beam and scanning electron instrument (FIB-SEM; FEI Helios Nanolab 600) incorporating an Oxford Instruments X-max 50 energy dispersive x-ray (EDX) detector was used for high-resolution surface imaging, specimen cross-section preparation and microanalysis, to characterise both features and corrosion layers at specimen surfaces. Scanning electron micrographs were acquired using an electron beam of energy 15 keV and current 0.34 nA. Ion-induced secondary electron images (FIB images) were acquired using a gallium ion beam of energy 30 keV and current 90 pA. Cross-sections were prepared using the gallium ion beam to mill trenches 20 µm x 10 µm in size and about 10 µm deep into the material. A beam current of 20 nA was used initially to excavate the trenches quickly. Further etching was then performed, scanning the beam in a line and advancing into the vertical cut face, at a beam current of 6.5nA to produce a smooth, clean, high-quality vertical surface free of redeposited material that could be examined using secondary electron imaging. Prior to trench excavation, platinum was deposited onto the surface using the electron and ion beams in conjunction with an organometallic gas transported to the surface through a needle injector close-by. This was to protect the surface while the trench was made, cutting through the deposit and into the substrate. Such platinum deposits are commonly used to study thin surface layers in order to make them easily visible and to prevent their removal during the initial imaging and etching stages [12]. The ion and electron columns on the instrument are arranged so that a cross-section of the specimen can be imaged using scanning electron microscopy during and after the trench is ion-milled.

The Magnox AL80 specimen that had been exposed to moist air without CO_2 possessed a corrosion layer that was too thick for trenching by ion-milling. Consequently, this specimen was mechanically sectioned to reveal the Magnox alloy/corrosion product interface in cross-section, and the FIB-SEM instrument was used to section across the interface and perpendicular to it so that a smooth, clean, high-quality surface was produced containing this interface. Secondary electron images were obtained of the region, and EDX gave chemical composition at discrete positions from one side of the interface to the other. Again, a platinum deposit was used prior to FIB cutting, to prevent uneven sputtering that can arise from rough surfaces.

2.4.5 Secondary ion mass spectrometry

Secondary ion mass spectrometry (SIMS) spectra, images and depth profiles were obtained using an in-house instrument comprising of an electronically variable aperture type gallium ion gun (FEI SD gallium LMIS EVA focusing column) fitted to a double focusing magnetic sector mass analyser (Vacuum Generators model 7035). The system vacuum during operation was $<10^{-7}$ mbar. The instrument was calibrated using values of $^m/_z$ = 68.93 for the backscattered Ga^+ ions. The instrument control software was 'Pisces' [13] operating under the Windows system.

Surface spectra were obtained by scanning a 25 keV gallium ion beam over an area ~400 µm square on the specimen while scanning the magnet to accept secondary ions in the range 0 Da to 100 Da, with a step size of 0.05 Da and a dwell time of 100 ms per step. Two sets of depth profiles were obtained. In the first, a

25 keV gallium ion beam of 3 nA current was scanned over an area 130 µm square. In the second, a 1 nA beam current was used over a close-by area 65 µm square. In both cases the species of interest detected were C^- ($^m/_z$ = 12), O^- ($^m/_z$ = 16), OH^- ($^m/_z$ = 17), C_2^- ($^m/_z$ = 24) and MgO^- ($^m/_z$ =4 0). A dwell time of 1 s was used for each species before repeating the cycle many times to obtain a depth profile over a time period of ten minutes. A Monte-Carlo computer program SRIM [14] was used to calculate the depth profiling rates of the ion beam under the two conditions adopted. The calculations assumed the material sputtered to be magnesium oxide (MgO) with a density of 3590 kg.m^{-3}. Gallium ions of 25 keV energy were inclined at a 45 ° angle of incidence to the substrate. The Monte-Carlo program simulates the trajectories of ions fired into the substrate, counting the number of atoms that escape from the surface, and hence calculating the rate of removal of material. The resulting calculation gave a volume sputtering rate of 0.96 µm^3.nC^{-1}. For the 3 nA beam current scanned over a 130 µm square, this gave a profiling rate of 7.7 nm.min^{-1}, while for the 1 nA beam current scanned over a 65 µm square, the resulting profile rate was 10.2 nm.min^{-1}. These calculations were applied to the depth profiling times to infer an erosion depth. A 'gating' facility rejected signals originating from the etch pit sidewalls, which would otherwise have caused loss of depth resolution [15].

3 RESULTS

3.1 Corrosion tests

The experimental programme began by exposing Magnox AL80, Magnox ZR55 and pure magnesium specimens to water vapour in flowing air. A subset of the specified test matrix of conditions was used: the notional water vapour concentrations and associated specimen temperatures are shown in Table 2. After a total exposure time of 126 days no mass gain was observed for any of the specimens, at or above the minimum detectable weight gain of 0.1 mg. Thus, assuming linear kinetics and that the corrosion product was $Mg(OH)_2$, the rate of reaction of magnesium could not have exceeded about 1.2x10^{-5} mgMg.m^{-2}.s^{-1}, where rate represents the mass of magnesium metal converted to hydroxide per unit surface area of the specimens per second. This result was unexpected, and thus the experimental programme was recast to find an explanation for this important observation. Thus all subsequent experiments used a notional specimen temperature of 90 °C. In addition, it was clear that the balance gas for the water vapour was having a significant effect, and thus the atmosphere was varied. In the main, specimens from the original experiment were included in the new test matrix, so they were not removed from the vessels. However, further specimens were introduced into this sequence of revised experimental conditions.

Figure 2 presents the measured Magnox AL80 specimen mass change rates as a function of time, together with the specific exposure condition adopted. For purposes of comparison, the individual data sets are presented with the same y-axis (rate of consumption of magnesium in units of mgMg.m^{-2}.s^{-1}). At intervals, specimens were removed from the reaction vessels, added to the vessels or transferred to different exposure conditions, as reflected in the mass histories of individual specimens. It is noteworthy that for the moist air containing CO_2 no measurable rate was observed. Figures 3 and 4 present the equivalent data for Magnox ZR55 and pure magnesium specimens, respectively. Please note that different x and y scale ranges are used in parts (a) and (b) of each of these figures.

The observed average corrosion rates are shown in Tables 3 and 4 for Magnox AL80, Tables 5 and 6 for Magnox ZR55 and Tables 7 and 8 for pure magnesium. The variety of experimental conditions makes

reporting of the observed rates in the Tables less than obvious; thus some explanation is needed. The corrosion rates are expressed as the weight loss of magnesium in $mgMg.m^{-2}.s^{-1}$, rather than the more usual $mg.dm^{-2}.d^{-1}$. In all of the Tables, the three columns on the left provide the period of exposure, the water vapour concentration and the test temperature. The rows that span the table contain the balance gas, either normal air, air from which the CO_2 had been removed or argon, applied during the periods tabulated below the row. The two columns to the right give the observed corrosion rates and reflect the introduction of new specimens at different times throughout the programme. If the entry in the rightmost column is blank, then new specimens had yet to be introduced. Those rates which are reported as 0.000, with no standard deviation in parentheses, were either less than the minimum detectable rate or did not differ statistically from zero. The single rate in the last two rows of Tables 3, 5 and 7 reflect that the existing and new specimens were treated as a single group. The measurements of corrosion rates obtained at the various conditions of temperature, water vapour pressure and gas composition are summarised in Figure 2 for Magnox AL80, Figure 3 for Magnox ZR55 and Figure 4 for pure magnesium. The test conditions are summarised in Table 9.

3.1.1 Dynamic tests

Magnox AL80

Table 3 demonstrates that no detectable corrosion rate was measured for the Magnox AL80 specimens tested in air containing water vapour. Removing CO_2 from the flowing air, however, produced a measurable rate of corrosion which was significantly greater in the second period of exposure. Changing the gas to high purity argon, which contained no CO_2, caused a further increase in corrosion rate. There was little difference in the observed rates between those specimens that had been exposed previously to moist air and those exposed to moist argon. There is no statistical difference between these rates and those in the two subsequent periods of exposure, where the water vapour concentration was increased slightly. Table 4 shows the effect of introducing Magnox AL80 specimens into moist air from which CO_2 has been removed. A significant corrosion rate was observed, higher than associated with argon, although the water vapour concentrations are greater. On changing to normal air containing CO_2, there was a marked reduction in corrosion rate, although it was not reduced to zero. The rate increases considerably in the subsequent exposure period, even though the water vapour concentration was less.

Magnox ZR55

The observed corrosion rates for Magnox ZR55 (Tables 5 and 6) show significant differences from those of Magnox AL80 and pure magnesium. The initial exposure to moist air produced no observable mass gain, but in the first period after changing to air containing CO_2 the observed average corrosion rate was not statistically different from zero. In the subsequent period of exposure the rate was similar to that for Magnox AL80 and pure magnesium. The rates in argon, whilst higher than in CO_2 air, were less than those of Magnox AL80 and pure magnesium. The greatest difference in behaviour is seen in Table 6, where the rate on exposure to CO_2-free air was almost zero. On introducing normal air, there is a barely significant increase in rate to a value similar to those measured for Magnox AL80 and pure magnesium respectively in Tables 4 and 8 (see below).

Pure magnesium

The observed corrosion rates for pure magnesium given in Tables 7 and 8 are very similar to those of the

Magnox AL80 specimens tested. The only significant difference is in Table 8 where the corrosion rate for specimens previously exposed to CO_2-free air is shown to be significantly greater than for those specimens subject to pre-exposure.

3.1.2 Static tests

In addition to dynamic tests, static tests were undertaken. When new specimens of either Magnox AL80, Magnox ZR55 or pure magnesium were exposed to moist gas (argon or CO_2-free air) at 90 °C gas temperature no mass gains were observed. When specimens of each alloy/metal that had previously been exposed to moist CO_2-free air and had experienced corrosion, leading to measured mass gains, were exposed further under static, moist argon conditions (again at 90 °C gas temperature) no further mass gains were observed.

3.1.3 Laboratory air conditions

Specimens of Magnox AL80, Magnox ZR5 and pure magnesium showed no significant mass gains after being exposed to laboratory air under ambient conditions for periods of 360 days.

3.2 Corrosion product formation

3.2.1 Morphology

Magnox AL80

Figures 5a and 5b compare the surface morphology of Magnox AL80 specimens after exposure to laboratory air and flowing moist CO_2-free air. The laboratory air exposed specimen shows presumed limited corrosion at grain boundaries (Figure 5a), even though there was no measurable mass gain after almost a year exposed to laboratory air under ambient conditions of temperature and humidity. The specimen exposed to a flowing moist CO_2-free air environment for four weeks at a temperature of 90 °C, with a mass gain of 7.8 mg, had a surface covered in µm-scale nodules (Figure 5b).

Magnox ZR55

Figures 5c and 5d compare the surface morphology of Magnox ZR55 specimens after exposure to laboratory air and flowing moist CO_2-free air. In contrast to as-cleaned specimens, the laboratory air exposed specimen shows a less-well defined surface (Figure 5c), even though there was no mass gain after almost a year exposed to laboratory air under ambient conditions of temperature and humidity. The specimen exposed to a flowing moist CO_2-free air environment for four weeks at a temperature of 90 °C had some small features, characteristic of the early stages of $Mg(OH)_2$ formation (Figure 5d), although again there was no measurable mass gain.

Pure magnesium

Figures 5e and 5f compare the surface morphology of pure magnesium specimens after exposure to laboratory air and flowing moist CO_2-free air. Grain boundaries visible in as-cleaned material were still visible in the laboratory air exposed specimen (Figure 5e). The specimen exposed to a flowing moist CO_2-free air environment for four weeks at a temperature of 90 °C, which did present a clear increase in mass, had a discoloured surface covered in nodules similar in size to those observed on the equivalent Magnox AL80 specimen, which we take to be $Mg(OH)_2$ (Figure 5f).

3.2.2 Crystal structure

<u>Magnox AL80</u>

XRD Θ/2Θ traces were recorded from separate examples of Magnox AL80 specimens removed from the reaction vessels. Figure 6a shows the diffraction trace after exposure to low relative humidity with CO_2 present in the gas stream (~90 °C vessel temperature; 182 days; no mass gain). By comparison, Figure 6b shows the trace after exposure for a short time at higher relative humidities (~90 °C vessel temperature; 28 days after introducing heated bubbler and removing the bypass, hence no CO_2). The phases identified from the diffraction traces are summarised in Table 10. The Magnox AL80 specimen analysed before any exposure to elevated humidity levels - i.e. before the introduction of heated bubblers, which, with the accompanying removal of the bypass lines around the bubblers, would also remove CO_2 from the gas stream - showed the presence of only metallic Mg peaks, within the detection limits of the technique. After a relatively short exposure to more moist conditions, hydride (MgH_2) and $Mg(OH)_2$ phases were observed in the diffraction traces. From the peak intensities, the proportion of $Mg(OH)_2$ increased after further exposure to high humidity, although MgH_2 peaks were then no longer evident.

<u>Magnox ZR55</u>

XRD Θ/2Θ traces were recorded from separate examples of Magnox ZR55 specimen removed from the reaction vessels after: (a) exposure for a short time at higher relative humidities (~90 °C vessel temperature; 28 days after introducing heated bubbler and removing the bypass, hence no CO_2; no mass gain); and (b) exposure for an extended time at higher relative humidities (~90 °C vessel temperature; 105 days after introducing heated bubbler and removing the bypass, hence no CO_2). No Magnox ZR55 specimen was removed to allow direct comparison with other specimens exposed only to the low humidity conditions. The phases identified from the diffraction traces are summarised in Table 10.

For the Magnox ZR55 specimen analysed after a relatively short exposure to moist conditions only metallic Mg peaks were seen in the diffraction trace. $Mg(OH)_2$ was observed after further exposure to high humidity. This trace is in agreement with the observed rates of mass gain for this material, in comparison to both Magnox AL80 and pure magnesium. However, although diffraction peaks for magnesium were observed as with Magnox AL80, the relative intensities of the peaks were different, indicative of preferred orientation in at least one of the materials. Such directional texture would be expected to be more likely for Magnox AL80 as this material was subject to severe hot-rolling.

<u>Pure magnesium</u>

XRD Θ/2Θ traces were recorded from separate examples of pure magnesium specimens removed from the reaction vessels after: (a) exposure only to low relative humidity with CO_2 present in the gas stream (~90 °C vessel temperature; 182 days; no mass gain); (b) exposure for a short time at higher relative humidities (~90 °C vessel temperature; 28 days after introducing heated bubbler and removing the bypass, hence no CO_2); and (c) exposure for an extended time at higher relative humidities (~90 °C vessel temperature; 105 days after introducing heated bubbler and removing the bypass, hence no CO_2). The phases identified from the diffraction traces are summarised in Table 10. The pure magnesium specimens behaved in a similar manner to the Magnox AL80 specimens, with only metallic Mg peaks being present after exposure to low humidity, followed by MgH_2 and $Mg(OH)_2$ after a short time at high humidity and $Mg(OH)_2$ only after extended times at high humidity. The diffraction peak intensities were consistent with the metallic magnesium remaining to a greater extent than for Magnox AL80, in line with mass gain data.

Particular searches were made for any evidence of peaks from MgO (periclase), $MgCO_3$ (magnesite) and other CO_3^--containing species in the x-ray diffraction data, but none was found. It should be remembered that the XRD sampling depth would be tens of micrometres. Any nm-scale films within the analysed volumes would be dominated by signals from the metallic substrate and/or hydroxide-based corrosion layer. Hence, SIMS was employed on Magnox AL80 following exposure to low relative humidity with CO_2 present in the gas stream (~90 °C vessel temperature; 182 days), to identify if $MgCO_3$ was present.

3.2.3   Composition (FIB-SEM, SIMS)

Magnox AL80

Figure 7 shows a scanning electron micrograph for a specimen exposed to moist air without CO_2, that had been mechanically sectioned and prepared using several grades of SiC papers. The dark region to the left of the image corresponds to the Magnox alloy, while the lighter region to the right is the corrosion product. EDX compositional analysis from positions 1 to 4 are presented below the micrograph. Position 1 corresponds to the Magnox alloy and shows the presence of magnesium and aluminium, as expected. The carbon is a result of contamination, possibly arising from interaction of the incident electron beam with the substrate surface in the presence of residual hydrocarbons from the pumping system. This artefact can be discounted. Positions 2 to 4 within the corrosion product show very similar results that are consistent with either magnesium oxide or hydroxide (it should be noted that EDX is unable to detect hydrogen). Figure 8 shows a scanning electron micrograph of the FIB-milled trench made across the metal-(hydr)oxide interface displaying the interface between the alloy and the rough corrosion layer. EDX microanalysis at nine positions across the sectioned region shows the Magnox alloy to the left (position 1) with a small amount of carbon attributable to system contamination, and oxide or hydroxide to the right. There is very little variation in composition from position to position within the corrosion product, indicating a homogeneous, solid coating that was approximately 60 μm thick. The 'flaring' in the image within the corrosion product to the upper right is a result of local charging.

SIMS depth profiles of a specimen exposed to low humidity air with CO_2 at 90 °C for 182 days are shown in Figure 9. The analyses were performed in negative SIMS mode, in which negative secondary ions are detected, using the instrument conditions described previously. The species monitored were: C^- ($^m/_z$ = 12), O^- ($^m/_z$ = 16), OH^- ($^m/_z$ = 17), C_2^- ($^m/_z$ = 24) and MgO^- ($^m/_z$ = 40). The curves of Figure 9 show the magnitudes of the signals obtained from these species as a function of sputtered depth, calculated from the Monte-Carlo program SRIM as mentioned previously. The measurements shown in Figure 9 were undertaken at two separate locations, termed area 1 and area 2. The vertical scale is 'Percentage of Full Scale', where the full scale values for each species are given in the legend. This is so that signals with greatly varying magnitudes can be presented conveniently on the same graph.

The SIMS technique is surface sensitive, giving signals from a depth of a few atom layers only, but the depth resolution in a profile is limited by several factors, including layer intermixing (due to implantation of the primary gallium ion beam) and the surface roughness of the specimen. From these depth profiles it can be inferred that several corrosion product layers are present at the surface of this Magnox AL80 specimen, but signals from the various layers are smeared and some interpretation is required. The carbon signal intensities (for both C^- and C_2^-) are high near the surface of the specimen, initially decrease over the depth

of 5 nm to 7 nm, come to a peak at 12 nm 15 nm, and then further decrease. The oxygen signal rises from its initial value at the surface, reaches a broad maximum and then declines. The broad maximum may in fact be comprised of two merged peaks. The positions of the two maxima are estimated to be at depths of 5 nm to 8 nm and at 15 nm to 20 nm. The OH^- signal rises from an initial value and peaks at a depth of 3 nm to 5 nm, before decaying. Finally, the MgO^- signal rises from a low value to a peak at a depth of 15 nm to 18 nm before decaying. There is also evidence of a 'shoulder' to the left of the main peak, consistent with a second peak at a depth of 8 nm to 10 nm. The overall thickness of the corrosion layer is approximately 25 nm to 35 nm, consistent with the FIB trench measurements. Similar trends are seen for both areas selected for analysis.

The depth resolution of the SIMS technique on this specimen is not quite sufficient to clearly resolve the individual thin corrosion product layers present, but it is enough to show that the corrosion layer is inhomogeneous with depth, and it is possible to estimate the order of the layers present. It is proposed that the data here are consistent with a layer of magnesium oxide (at the Magnox alloy surface), followed by a layer of magnesium carbonate, then a layer containing magnesium hydroxide and finally a layer of carbon-containing contaminant at the surface. The carbon SIMS signals are higher at the surface (corresponding to the contaminant layer), decreasing as the hydroxide layer is encountered, rising again at the carbonate layer and then decaying as the oxide and alloy are reached. The oxygen signal is high in the hydroxide and oxide layers, reducing slightly in the intermediate carbonate layer, and then decaying into the bulk alloy. The OH^- signal peaks at the hydroxide layer and, finally, the MgO^- signal is strongest at the magnesium oxide layer, with a smaller contribution from the carbonate layer. A schematic of the proposed corrosion product layer structure is presented in Figure 10. With the depth resolution achieved, the measured distributions of the elements (Figure 9) obtained are consistent with this structure, but it is possible that the structure is more complex, containing localised features that are not resolved.

4   DISCUSSION

The most significant observation in these experiments is the marked dependency of the corrosion rates on the composition of the balance gas containing water vapour. Corrosion was suppressed in natural air, whilst the corrosion rates for Magnox AL80 in moist argon were similar to those found by Parsons and Friskney [4]. The experiments demonstrate that removing CO_2 from the balance gas removes the inhibition of corrosion and that the partial removal of CO_2, to give lower concentrations than the ~400 vppm in natural air, reduces the corrosion rate but does not suppress it entirely, at least at higher humidities. The mechanisms of either suppression or inhibition of corrosion are maintained for the specific conditions, namely the presence of CO_2 in the moist air. Figures 2a, 3a and 4a show that specimens of each of the materials selected exposed for six months (182 days) in an atmosphere containing CO_2 start corroding once the CO_2 is removed. However, once corrosion is proceeding, the reintroduction of CO_2 inhibits or suppresses the corrosion process (Figures 2b, 3b and 4b). These observations of the role of CO_2 in moist air on the corrosion of Magnox AL80 or pure magnesium are consistent with data obtained by the CEGB and by its contractors that showed rates of corrosion of Magnox AL80 in steam at pressures in excess of one atmosphere were slower in pure CO_2 than in air [16]. Experiments in which pure magnesium was exposed to moist ambient air [17] show an inhibition of the corrosion rate by CO_2 gas. As far as we can determine, however, the present tests have produced the first experimental measurements made where the CO_2 in natural air has suppressed breakaway corrosion completely. These results are of considerable

significance for the storage of Magnox alloy fuel elements in air-filled reactors and demonstrate the potential to invoke operational simplifications with a consequent reduction of cost. It is, therefore, important to consider whether these observations are consistent with the understanding of the kinetics and mechanisms of Magnox alloy corrosion.

We now explore the mechanisms that would lead to the inhibition of breakaway corrosion of pure magnesium and its alloys by CO_2 gas in the proportions encountered in moist air. There are two potential corrosion reactions:

$$Mg + H_2O \rightarrow MgO + H_2 \tag{2}$$
$$Mg + 2H_2O \rightarrow Mg(OH)_2 + H_2 \tag{3}$$

Which of these reactions is controlling depends on the equilibrium of the reaction:

$$Mg(OH)_2 \rightleftharpoons MgO + H_2O \quad (\Delta H^0_{298} = 81.1 kJ.mol^{-1} \text{ [18]}) \tag{4}$$

By application of Le Chatelier's principle to the endothermic reaction (4), high humidity drives it to the left and high temperature drives it to the right. As a consequence, the formation of MgO is favoured at low humidity and higher temperatures. Thus, all the conditions of water vapour pressure and temperature used in this study will favour the formation of $Mg(OH)_2$ (brucite), which has a layer structure [19] and a lower density than MgO (periclase). It is known that periclase is relatively protective (see, for example, reference 4) and thus the reaction rate is limited by the rate of diffusion of magnesium atoms through the oxide layer. Brucite, in contrast, is less protective as it cracks and spalls under the residual stresses arising from oxide growth and thus provides little resistance to the transport of oxidising species.

The XRD data (Figure 6) show that the corrosion products are entirely $Mg(OH)_2$, with occasional traces of MgH_2. This is consistent with expectations from the thermodynamic analysis of reaction (3). Thermodynamics, however, do not permit a layer of $Mg(OH)_2$ on magnesium metal as the $Mg(OH)_2$ will disproportionate [18]:

$$Mg + Mg(OH)_2 \rightleftharpoons 2MgO \tag{5}$$

The corrosion product on the metal surface is MgO. X-ray photoelectron spectroscopy (XPS) studies of the initial stages of magnesium corrosion in water vapour [5-7] show the presence of a thin layer (~10nm) formed by semi-logarithmic kinetics (Figure 9). The corrosion layers found in these experiments are of the order of micrometres thick (implying linear kinetics) and, thus, it is not surprising that MgO was not detected by XRD beneath the hydroxide. Certainly, Parsons and Friskney [4] detected MgO at higher temperatures than employed in these experiments, where the corrosion product layers are thinner. The diffusion coefficient of Mg in MgO is more than two orders of magnitude greater than that of the oxygen anion [20]. Therefore, the MgO layer grows by addition of oxygen at the MgO/gas interface. In pure water vapour the overall reaction is given by reaction (2). In moist air there is the possibility that di-oxygen suppresses the reaction with water vapour, as observed in uranium [21] at similar temperatures to those used in this study, and so magnesium reacts with di-oxygen with no production of hydrogen. There is evidence that hydrogen is produced by the reaction of magnesium with liquid water and, thus, presumably with water vapour at partial pressures approaching the saturated water vapour pressure. Whether the reaction is with either water vapour or oxygen at the humidities employed in this study is of little consequence for the overall mechanism. However, if hydrogen is produced it would be of significance, particularly for storage of Magnox alloy fuel elements. When breakaway corrosion occurs, the upper surface of the growing layer of

MgO is hydrolysed to $Mg(OH)_2$ [22]. The layer structure of $Mg(OH)_2$ (brucite) offers no barrier to water vapour (or oxygen) and, thus, the reaction occurs at the $MgO/Mg(OH)_2$ interface (Figure 10). The formation of such a dual layer has been observed by XPS [23] and the activation energy for the hydrolysis of MgO is similar to that found by Friskney at al [22] for the corrosion of Magnox alloy in water vapour. The corrosion rate in the breakaway regime is given by the rate of hydrolysis of MgO and the thickness of the MgO layer next to the metal is such that the rate of production of MgO is equal to the rate of hydrolysis.

The corrosion and protection of magnesium alloys has been the subject of much recent research to increase the corrosion resistance for biomedical applications and in the transportation industry, where fuel efficiencies can arise from reduced masses. (See reviews by Gusieva et al [24], Tan et al [25], Atrens et al [26] and Taheri et al [27].) There is a greater emphasis on corrosion in aqueous conditions, rather than in the relatively dry atmosphes in this study. Nevertheless, it is found that surface films identified in aqueous conditions and the present results in moist air are similar in that both comprise a thin MgO inner layer and a thicker $Mg(OH)_2$ outer layer, and that the outer layer thickens by hydration of the inner [27, 28].

It is noteworthy that Parson and Friskney [4], when measuring corrosion rates as a function of relative humidity, observed a change in slope for rates at a relative humidity of about 0.15, while for rates below this humidity they were independent of temperature, within the range considered. A similar discontinuity occurs in the hydrolysis of MgO [29], but at a relative humidity of about 0.3. It is proposed that these values correspond with the formation of a monolayer of water. At higher relative humidities, multiple layers of water can form by condensation of successive monolayers of water. It is noteworthy that the rate is apparently a function of the number of layers of absorbed water; the rate should become constant when the number of layers of absorbed water is sufficient to act as bulk water. It is considered that aqueous films that are thicker than three monolayers possess properties that are close to those of bulk water [30]. It can be shown from the expression for the BET absorption isotherm [31] (assuming the average heat of absorption of the first layer is equal to the heat of liquefaction) that three monolayers occur when the relative humidity exceeds approximately 75 %. The measurements of Parsons and Friskney [4] were carried out at relative humidities of less than 70 %. In contrast, the measurements of Lindstrom et al [17] used relative humidities of about 95 %, where they estimated that there were more than 16 monolayers present. The conditions employed in experiments reported here were deliberately chosen to be below known rate discontinuities, where it might be expected that that sub-monolayers of water are formed at the $MgO/Mg(OH)_2$ interface. The observed rates in the absence of inhibition are shown in Tables 3 to 8 and Figures 2 to 4. Some limited kinetic information can be extracted from these data.

Turning now to the mechanism of inhibition by CO_2, there is very little information in the open literature that is relevant to the conditions used here. Fotea et al [23] inferred from XPS data that a layer of $MgCO_3$ forms on the surface of the $Mg(OH)_2$ nearest to the ambient atmosphere. Abreu et al [32] used x-ray photoelectron spectroscopy to show that an as-received sample of commercial magnesium that had been exposed to ambient air contained a surface covered by a film predominantly consisting of magnesium hydroxide and a smaller but appreciable quantity of magnesium bicarbonate. They concluded from a comparison of the areas under the O1s and C1s peaks that less than 25 % of the bicarbonate existed in the surface layers. Lindström et al [17] showed that the corrosion rate for magnesium in air was inhibited by CO_2 at a temperature of 22 °C and relative humidity of 95 %. Under these conditions, the specimens in 350 ppm CO_2 reached a constant weight gain of about 20 $\mu g.cm^{-2}$ after 180 hr (7.5 days) exposure. There is a

suggestion that after a total of 700 hr (29.2 days) exposure the weight gain started to increase again. Lindström et al [17] were unable to detect the presence of crystalline carbonate compounds by XRD. These workers were, however, able to analyse for carbonate by measuring the evolution of CO_2 after dissolution in 20 % chromic acid. From this, and the mass gain measurements, they inferred the presence of a surface film of artinite ($Mg_2(OH)_2CO_3 \cdot 3H_2O$) 84 nm thick. There is an important difference between the experiments described here and those of Lindström et al [17] in that the relative humidity in the latter was 95 %. At this humidity it would be expected that there will be multiple layers of adsorbed water on the magnesium which will act as bulk water. This will dissolve CO_2 gas and, thus, the magnesium will be reacting, in effect, with carbonic acids. In contrast, it is expected that the adsorbed water in these experiments will be sub-monolayer (as the relative humidity is less than 0.3) and thus the surface chemistry will be markedly different. Although these results suggest that magnesium alloys will not undergo breakaway corrosion in moist air at low relative humidities, there are many observations of hydrogen generation from Magnox alloy debris in damp storage facilities. It may be that these corrosion reactions are occurring in liquid water that has entered the vault, in water condensed onto the cold debris or at higher relative humidities than employed in these studies. It does, however, demonstrate that the suppression of corrosion observed in these experiments will not necessarily be observed at higher humidities.

The SIMS results (Figure 9) have shown that the structure of the corrosion product formed on Magnox AL80 from moist air containing CO_2 is multi-layered and contains carbon, most likely as carbonates. It is straightforward to show from thermodynamics [18] that $MgCO_3$ cannot exist in equilibrium with magnesium metal. This is also the case for $Mg(OH)_2$, The layer adjacent to the magnesium surface must, therefore, be MgO. White has given an isothermal phase diagram for the system $MgO-CO_2-H_2O$ system in the solid-vapour region at 25 °C [33]. This diagram shows that at an atmospheric concentration of 400 ppm CO_2 the only phase present at water concentrations of about 3000 ppm and below is magnesite ($MgCO_3$). Above this water concentration the stable phase is hydromagnesite ($4MgCO_3.Mg(OH)_2.4H_2O$). Once the CO_2 concentration falls below 10 ppm brucite ($Mg(OH)_2$) becomes the stable phase, and then only with water vapour concentrations in excess of 1500 ppm. For the water vapour concentrations used in this study (in excess of 20000 ppm) the stable phase is expected to be hydromagnesite.

X-ray diffraction identified traces of MgH_2 present in some of the specimens (Table 9), similar to the findings of Parsons and Friskney [4]. It is not apparent from the SIMS data where the magnesium hydride is located within the surface layers. Brady et al [11] found penetration of hydrogen into the underlying metal after exposure of magnesium to humid air at 85 °C and so it seems likely that this is the location of the MgH_2 found in this study.

It is postulated that the uppermost layer of corrosion product (Figure 10) is more likely to be hydromagnesite, rather than magnesium hydroxide. Note that hydromagnesite contains both magnesium hydroxide and water of crystallisation and can generate the hydroxide to a depth derived from SIMS data (Figure 9). The failure to observe measurable corrosion in moist air, in contrast to measurable linear kinetics in the absence of CO_2, implies that magnesite and hydromagnesite, unlike brucite, form protective layers which prevent breakaway corrosion. The usual explanation for breakaway corrosion is that compressive stresses cause the oxide layer to spall before reaching the critical thickness at which parabolic kinetics fall to a negligible rate. The structures of hydromagnesite [34] and magnesite [35] are described as three-dimensional structures of MgO_6 octahedra and triangular carbonate ions. Brucite, in contrast, is a

layered structure [19], where the layers are held together by hydrogen bonding. It is proposed that the magnesite structures, held together by ionic bonds, resist the compressive stresses arising from corrosion and can form a fully protective layer, unlike the weaker brucite structure. In the absence of CO_2, the stable phase becomes brucite in the presence of water vapour. White [33] reports that CO_2 will react with brucite to form magnesite so the reverse reaction, the hydrolysis of magnesium carbonate to brucite, can also occur. This is consistent with the present observation that exposing specimens to an atmosphere with no CO_2, following prior exposure to moist air, leads to breakaway kinetics as the protective layer is hydrolysed. The gradually increasing corrosion rate with exposure time that is observed is consistent with a progressive thinning of the carbonate layer. As a consequence, there is a mechanistic basis that explains the observed corrosion kinetics in moist air either containing CO_2 or with CO_2 removed.

5   CONCLUSIONS

It may be concluded that when pure magnesium and the commercial magnesium alloys, Magnox AL80 and Magnox ZR55, were exposed to moist air there was no evidence of breakaway oxidation. It is proposed that the corrosion kinetics observed are a consequence of the formation of a protective layer of magnesium carbonate. The presence of this carbonate layer is supported by the secondary ion mass spectrometry measurements undertaken on the surface corrosion products. In the case of exposure in moist argon (hence, no CO_2 present), the magnesium and proprietary alloys, Magnox AL80 and Magnox ZR55, exhibit breakaway corrosion with linear kinetics. In this case, the corrosion product was essentially $Mg(OH)_2$ and there was no evidence of the presence of a protective layer. Similarly, when CO_2 is removed from the moist air linear breakaway corrosion is observed for these materials. Again, in the latter cases where breakaway corrosion occurs, there is no evidence for the inhibiting corrosion product. Finally, these data reveal that it is possible to inhibit breakaway corrosion by the reintroduction of moist air containing CO_2. As a consequence, exposure of the Magnox alloys to warm (temperatures less than 90 °C) moist air will not lead, over extended periods of time, to significant corrosion.

6   ACKNOWLEDGEMENTS

7   REFERENCES

[1]   M.R. Wootton, R. Moskovic, C.J. Bolton, P.E.J. Flewitt, Magnox steel reactor pressure vessel monitoring schemes: An overview, Journal of ASTM International 7 (2010) 1-15.

[2]   L.M. Wyatt, Materials of Construction for Steam Power Plant, Applied Science, London, 1976.

[3]   C.A. Friskney, The corrosion of etched Magnox Al-80 in dry steam at ~10^5 Pa pressure in the temperature range 373-573 K, J. Nucl. Mater. 99 (1981) 165-172.

[4]   W.T. Parsons, C.A. Friskney, The corrosion of etched Al-80 in water vapour, CEGB Report TPRD/B/0433/N84, March 1984 (available upon request to the authors).

[5]   T. Do, S.J. Splinter, C. Chen, N.S. McIntyre, The oxidation kinetics of Mg and Al surfaces studied by AES and XPS, Surf. Sci. 387 (1997) 192-198.

[6]   N.S. McIntyre, C. Chen, Role of impurities on Mg surfaces under ambient exposure conditions, Corros. Sci. 40 (1998) 1697-1709.

[7]   S.J. Splinter, N.S. McIntyre, W.N. Lennard, K. Griffiths, G. Palumbo, An AES and XPS study of the initial oxidation of polycrystalline magnesium with water vapour at room temperature, Surf. Sci. 292 (1993) 130-144.

[8]   S. Feliu Jr, A. Pardo, M.C. Merino, A.E. Coy, F. Viejo, R. Arrabal, Correlation between the surface chemistry and the atmospheric corrosion of AZ31, AZ80 and AZ91D magnesium alloys, Appl. Surf. Sci. 255 (2009) 4102-4108.

[9]   S. Feliu Jr, M.C. Merino, R. Arrabal, A.E. Coy, E. Matykina, XPS study of the effect of aluminium on the atmospheric corrosion of the AZ31 magnesium alloy, Surf. Interface Anal. 41 (2009) 143-150.

[10]   S. Feliu Jr, C. Maffiotte, J.C. Galván, A. Pardo, M.C. Merino, The application of x-ray photoelectron spectroscopy in understanding corrosion mechanisms of magnesium and Mg-Al alloys, The Open Surface Science Journal 3 (2011) 1-14.

[11]   M.P. Brady, M. Fayek, H.M. Meyer III, D.N.Leonard, H.H. Elsentriecy, K.A. Unocic, L.M. Anovitz, E. Cakmak, J.R. Kieser, G.L.Song, B. Davis, Tracer study of oxygen and hydrogen uptake by Mg alloys in air with water vapour, Scripta Materialia 106 (2015) 38-41.

[12]   T. Tao, J.S. Ro, J. Melngailis, Z. Xue, H.D. Kaesz, Focused ion beam induced deposition of platinum, J. Vac. Sci. Technol. B 8 (1990) 1826-1829.

[13]   J.C.C. Day, Daytasystems Limited, UK, http://www.daytasystems.co.uk/spectrometercontrol/index.php/contact (accessed 04.01.16).

[14]   J.F. Ziegler, M.D. Ziegler, J.P. Biersack, SRIM - The stopping and range of ions in matter, Nucl. Instrum. Meth. B 268 (2010) 1818-1823.

[15]   K. Wittmaack, p649 In: O. Meyer, G. Linker, F. Kappeler (editors) Proceedings of the Second International Conference on Ion Beam Surface Layer Analysis, Plenum Press, New York, 1976.

[16]   C.A. Friskney, The corrosion of Magnox alloys in moist carbon dioxide under pressure, CEGB Report TD/FCB/MEM/1103, October 1991 (available upon request to the authors).

[17]   R. Lindström, L.-G. Johansson, G.E. Thompson, P. Skeldon, J.-E. Svensson, Corrosion of magnesium in humid air, Corros. Sci. 46 (2004) 1141-1158.

[18]   O. Kubaschewski, E.LI.Evans, C.B.Alcock, Metallurgical Thermochemistry, 4th Edition, Pergamon Press, Oxford, 1967.

[19]   B.G. Hyde, S. Andersson, Inorganic Crystal Structures, pp137-138, Wiley-Interscience, New York, 1989.

[20]   P. Kofstadt, Nonstoichiometry, Diffusion and electrical conductivity in binary metal oxides, p121, Wiley-Interscience, New York, 1972.

[21]   C.A. Colmenares, Oxidation mechanisms and catalytic properties of the actinides, Prog. Solid State Ch. 15 (1985) 257-364.

[22]   C.A. Friskney, R.J. Pearce, I.H. Robins, K.A. Simpson, A.B.J. Cutler, C.J. Grant, B. Case, P.M. Bradford, The corrosion of Magnox Al-80 alloy in aqueous and moist environments, pp77-82, in Gas-Cooled Reactors Today (Volume 1) Proceedings of the Conference held in Bristol on 20-24 September 1982, British Nuclear Energy Society, London.

[23]   C. Fotea, J. Callaway, M.R. Alexander, Characterisation of the surface chemistry of magnesium exposed to the ambient atmosphere, Surf. Interface Anal. 38 (2006) 1363-1371.

[24]   K. Gusieva, C.H.J. Davies, J.R. Scully, N. Birbilis, Corrosion of magnesium alloys: The role of alloying, Int. Mater.Rev. 60 (2015) 169-194.

[25]   Q. Tan, A. Atrens, N. Mo, M.-X. Zhang, Oxidation of magnesium alloys at elevated temperatures in air: A review, Corros. Sci. (2016), http://dx.doi.org/10.1016/j.corsci.2016.06.018

[26]   A. Atrens, G-L. Song, M. Liu, Z. Shi, F. Cao, M.S. Dargusch, Advanced Engineering Materials 17 (2015) 400-453.

[27]   M. Taheri, R.C. Phillips, J.R. Kish, G.A. Button, Analysis of the surface film formed on Mg by exposure to water using a FIB cross-section and STEM-EDS, Corros. Sci. 59 (2012) 222-228.

[28]   M. Taheri, M. Danale, J.R. Kish, TEM examination of the film formed on corroding Mg prior to breakdown, J. Electrochem. Soc. 161 (2014) C89-C94.

[29]   G.K. Layden, G.W. Brindley, Kinetics of vapor-phase hydration of magnesium oxide, J. Am. Ceram. Soc. 46 (1963) 518-522.

[30]   C. Laygraf, T. Graedel, Atmospheric Corrosion, Wiley-Interscience, New York, 2000.

[31]   V.R. Williams, W.L. Mattice, H.B. Williams, Basic Physical Chemistry for the Life Sciences, 3rd edition, p432, WH Freeman, San Francisco, 1978.

[32]   J.B. Abreu, J.E. Soto, A. Ashley-Facey, M.P. Soriaga,J.F. Garst, J.L. Stickney, The interfacial chemistry of the Grignard reaction: The composition of the film formed on air-exposed magnesium, J. Colloid Interf. Sci. 206 (1998) 247-251.

[33]   R.B. White, Thermodynamic equilibrium, kinetics, activation barriers, and reaction mechanisms for chemical reactions in Karst Terrains, Environ. Geol. 30 (1997) 46-58.

[34]   M. Akao, F. Marumo, S. Iwai, The crystal structure of hydromagnesite, Acta Crystallogr. B 30 (1974) 2670-2672.

[35]   K. Dong Oh, H. Morikawa, S. Iwai, H. Aoki, Hydrothermal growth of magnesite single crystals, Am. Mineral. 58 (1973) 339-340.

[36]   D.J. Hodkin, P.G. Mardon, The diffusion of plutonium in magnesium and magnesium alloys, J. Nucl. Mater.16 (1965) 271-289.

[37]   Goodfellow Cambridge Limited, personal communication (2016).

Table 1. Composition of source magnesium alloys and pure magnesium used as raw material for the manufacture of specimens in this study.

Alloy	Element (wt%)												
	Be	Al	Si	Ca	Mn	Fe	Ni	Cu	Zn	Zr	Sn	Bi	Mg
Magnox AL80 [36]	0.003	0.8	<0.008	<0.005	<0.005	<0.005	—	<0.005	0.008	—	<0.005	<0.002	Balance
Magnox ZR55 [34]	—	<0.02	<0.01	<0.008	<0.01	<0.006	—	<0.01	0.008	0.5	<0.01	<0.005	Balance
Pure magnesium [37]	—	0.01	0.009	—	0.002	0.002	0.001	<0.001	<0.001	—	—	—	Balance

Table 2. Notional water vapour concentration and associated specimen temperature conditions during first 126 days of exposure.

Nominal water concentration (vppm)	Specimen temperature (°C)
200	40
200	50
20000	70
20000	90

Table 3. Exposure history and observed average corrosion rates of Magnox AL80 specimens under a variety of exposure conditions (part 1).

Period (d)	Water concentration (vppm)	Specimen temperature (°C)	Corrosion rate (mgMg.m^{-2}.s^{-1})	Corrosion rate (mgMg.m^{-2}.s^{-1})
Air, CO$_2$				
126	20000	92	0.000	—
22	49300	91	0.000	—
34	54300	91	0.000	—
Air, no CO$_2$				
28	55200	91	0.0017 (0.0011)	—
77	64700	89	0.013 (0.003)	—
Argon				
30	55000	86	0.0030 (0.0012)	—
33	64700	89	0.0044 (0.0017)	
42	64500	92	0.0030 (0.0010)	

Table 4. Exposure history and observed average corrosion rates of Magnox AL80 specimens under a variety of exposure conditions (part 2).

Period (d)	Water concentration (vppm)	Specimen temperature (°C)	Corrosion rate (mgMg.m^{-2}.s^{-1})	Corrosion rate (mgMg.m^{-2}.s^{-1})
Air, no CO_2				
30	74800	89	0.0051 (0.0002)	—
33	80700	90	0.0060 (0.0022)	—
Air, CO_2				
42	66600	90	0.0008 (0.0001)	0.0008 (0.0004)
228	41800	90	0.0011 (0.0010)	

Table 5. Exposure history and observed average corrosion rates of Magnox ZR55 specimens under a variety of exposure conditions (part 1).

Period (d)	Water concentration (vppm)	Specimen temperature (°C)	Corrosion rate (mgMg.m^{-2}.s^{-1})	Corrosion rate (mgMg.m^{-2}.s^{-1})
Air, CO_2				
126	20000	92	0.000	—
22	49300	91	0.000	—
34	54300	91	0.000	—
Air, CO_2				
28	55200	91	0.00004 (0.00004)	—
77	64700	89	0.0073 (0.0011)	—
Argon				
30	55000	86	0.0010 (0.0009)	—
33	64700	89	0.0009 (0.0008)	
42	64500	92	0.0017 (0.0010)	

Table 6. Exposure history and observed average corrosion rates of Magnox ZR55 specimens under a variety of exposure conditions (part 2).

Period (d)	Water concentration (vppm)	Specimen temperature (°C)	Corrosion rate (mgMg.m^{-2}.s^{-1})	Corrosion rate (mgMg.m^{-2}.s^{-1})
Air, no CO_2				
30	74800	89	0.000	—
33	80700	90	0.0008 (0.0002)	—
Air, CO_2				
42	66600	90	0.0012 (0.0001)	0.000
228	41800	90	0.0012 (0.0002)	

Table 7. Exposure history and observed average corrosion rates of pure magnesium specimens under a variety of exposure conditions (part 1).

Period (d)	Water concentration (vppm)	Specimen temperature (°C)	Corrosion rate (mgMg.m^{-2}.s^{-1})	Corrosion rate (mgMg.m^{-2}.s^{-1})
Air, CO$_2$				
126	20000	92	0.000	—
22	49300	91	0.000	—
34	54300	91	0.000	—
Air, no CO$_2$				
28	55200	91	0.0017 (0.0013)	—
77	64700	89	0.0087 (0.003)	—
Argon				
30	55000	86	0.0016 (0.0005)	0.0022 (0.0001)
33	64700	89	0.0050 (0.0022)	
42	64500	92	0.0031 (0.0017)	

Table 8. Exposure history and observed average corrosion rates of pure magnesium specimens under a variety of exposure conditions (part 2).

Period (d)	Water concentration (vppm)	Specimen temperature (°C)	Corrosion rate (mgMg.m^{-2}.s^{-1})	Corrosion rate (mgMg.m^{-2}.s^{-1})
Air, no CO$_2$				
30	74800	89	0.0051 (0.0002)	—
33	80700	90	0.0056 (0.0002)	—
Air, CO$_2$				
42	66600	90	0.0028 (0.0001)	0.0008 (0.0007)
228	41800	90	0.0016 (0.0002)	

Table 9. Summary of exposure conditions employed in corrosion tests: ✗ no breakaway corrosion observed; ✓ breakaway corrosion observed; 'initiation' measurable corrosion only seen after a period of exposure to the reactive conditions; — not applicable.

Material	90 °C															
	Air								Argon							
	With CO$_2$				Without CO$_2$				With CO$_2$				Without CO$_2$			
	Flowing		Static		Flowing		Static		Flowing		Static		Flowing		Static	
	Dry	Moist	Dry	Moist	Dry	Moist	Dry	Moist	Dry	Moist	Dry	Moist	Dry	Moist	Dry	Moist
Magnox Al80	—	✗	—	✗	—	✓	✗	—	—	—	—	—	—	✓	✗	—
Magnox Zr55	—	✗	—	✗	—	✓ initiation	✗	—	—	—	—	—	—	✓ initiation	✗	—
Pure magnesium	—	✗	—	✗	—	✓	✗	—	—	—	—	—	—	✓	✗	—

Table 10. Phases identified on specimen surfaces, using x-ray diffraction, following exposure to the indicated conditions, together with links to representative scanning electron micrographs and mass change rate charts.

Material	Exposure conditions	Phases identified	Example micrographs	Mass change rate
Magnox AL80	90 °C; Air; Moist; CO_2; 182 d	Mg	—	Figure 2a
Magnox AL80	90 °C; Air; Moist; no CO_2; 28 d	Mg; MgH_2; $Mg(OH)_2$	Figure 5b	Figure 2a
Magnox AL80	90 °C; Air; Moist; no CO_2; 105 d	Mg; MgH_2; $Mg(OH)_2$	—	Figure 2a
Magnox ZR55	90 °C; Air; Moist; CO_2; 182 d	—	—	—
Magnox ZR55	90 °C; Air; Moist; no CO_2; 28 d	Mg	Figure 5d	Figure 3a
Magnox ZR55	90 °C; Air; Moist; no CO_2; 105 d	Mg; $Mg(OH)_2$	—	Figure 3a
Pure magnesium	90 °C; Air; Moist; CO_2; 182 d	Mg	—	Figure 4a
Pure magnesium	90 °C; Air; Moist; no CO_2; 28 d	Mg; MgH_2; $Mg(OH)_2$	Figure 5f	Figure 4a
Pure magnesium	90 °C; Air; Moist; no CO_2; 105 d	Mg; $Mg(OH)_2$	—	Figure 4a

Mg, hexagonal, a = 3.21 Å, c = 5.21 Å, e.g. ICDD 35-0821;

MgH_2, tetragonal, a = 4.52 Å, c = 3.02 Å, e.g. ICDD 12-0697;

$Mg(OH)_2$, hexagonal, a = 3.14 Å, c = 4.78 Å, e.g. ICDD 44-1482;

MgO, cubic, a = b = c = 4.2 Å, e.g. ICDD 87-0653;

$MgCO_3$, rhombohedral, a = b = 4.65 Å, c = 15.2 Å, e.g. ICDD 86-2348.
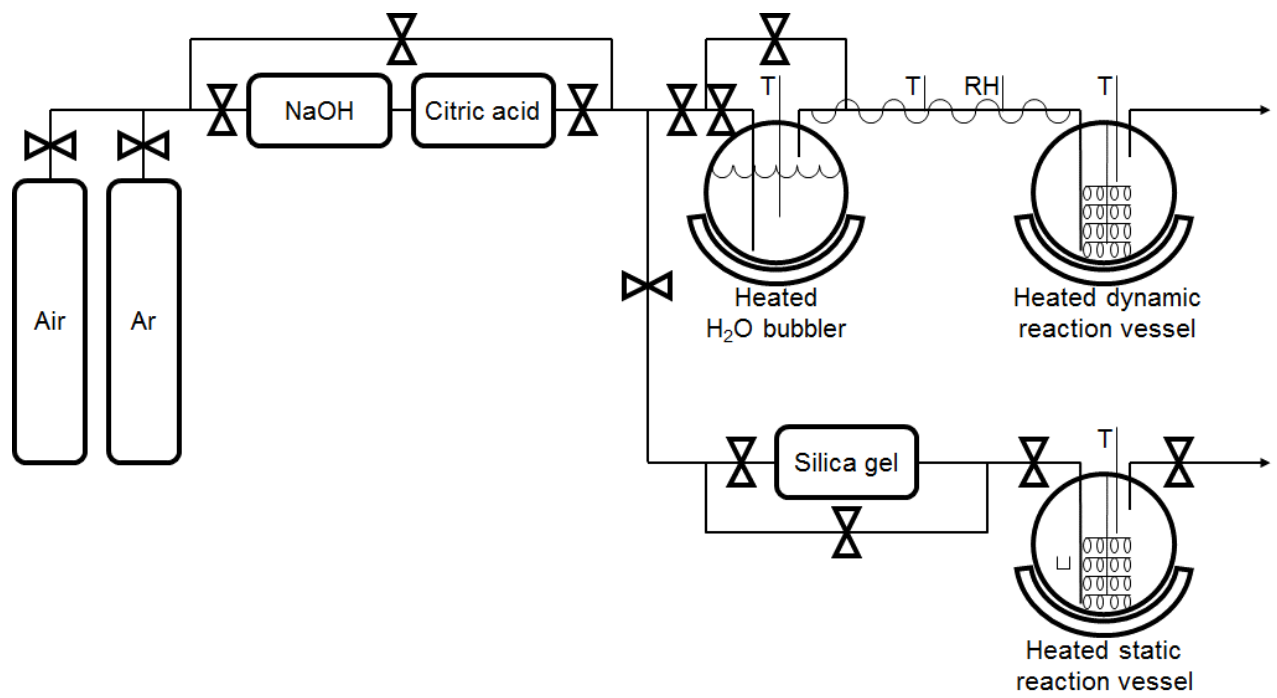
Figure 1. Full corrosion exposure rig schematic diagram showing the arrangement of the reaction vessels to allow dynamic and static tests to be undertaken.
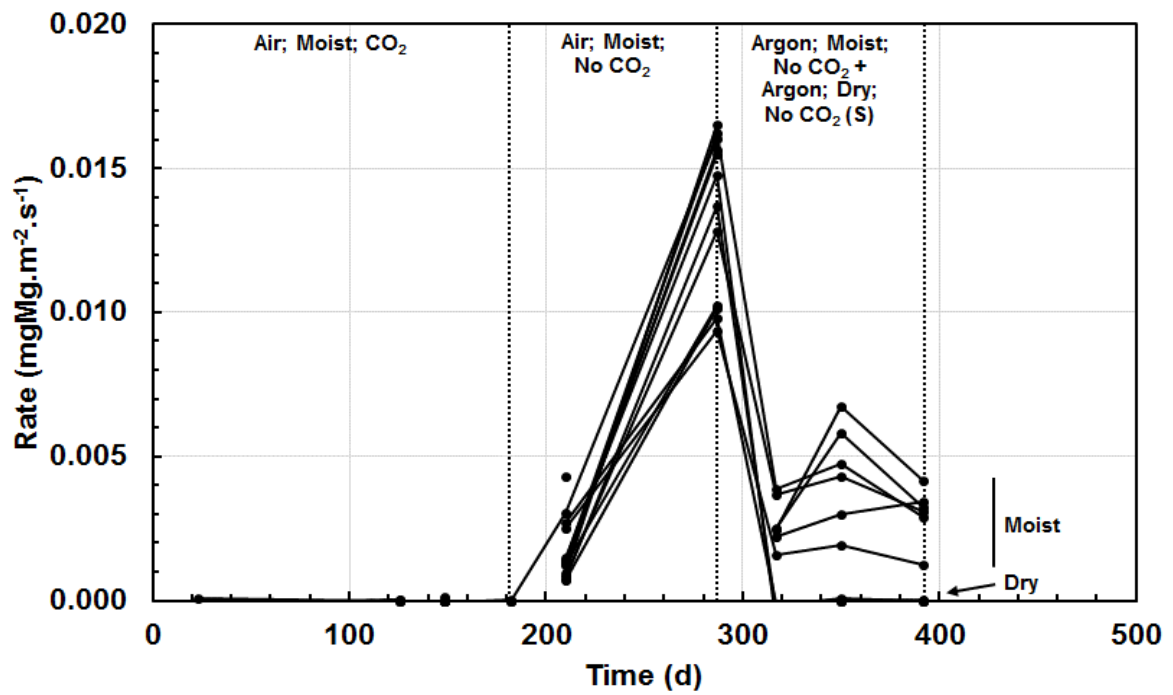
(a)
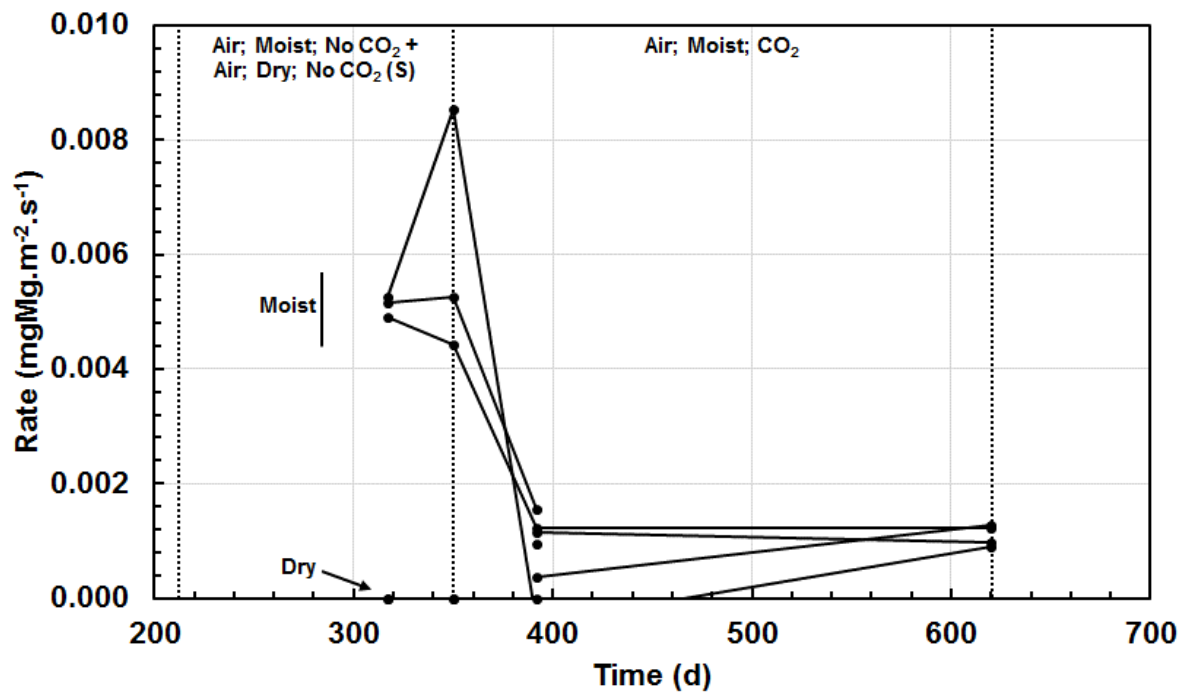
(b)

Figure 2. Measured corrosion rates for multiple individual Magnox AL80 specimens under exposure conditions indicated, highlighting trends and variability. Please note that different x and y scale ranges are used in (a) and (b).
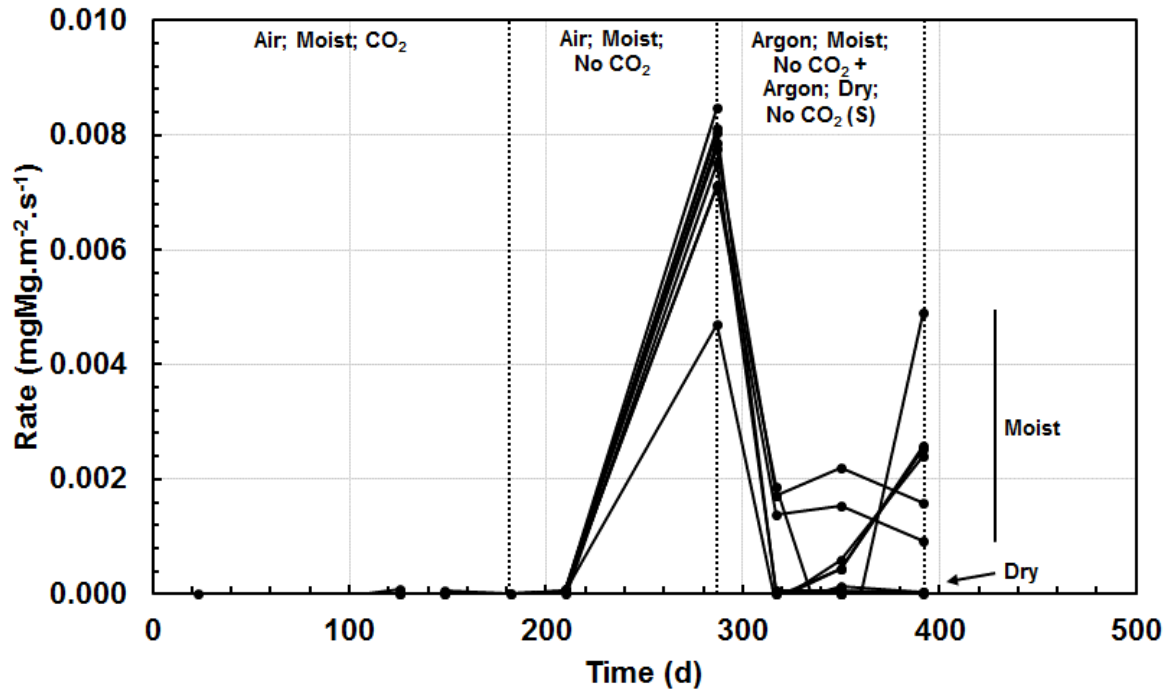
(a)
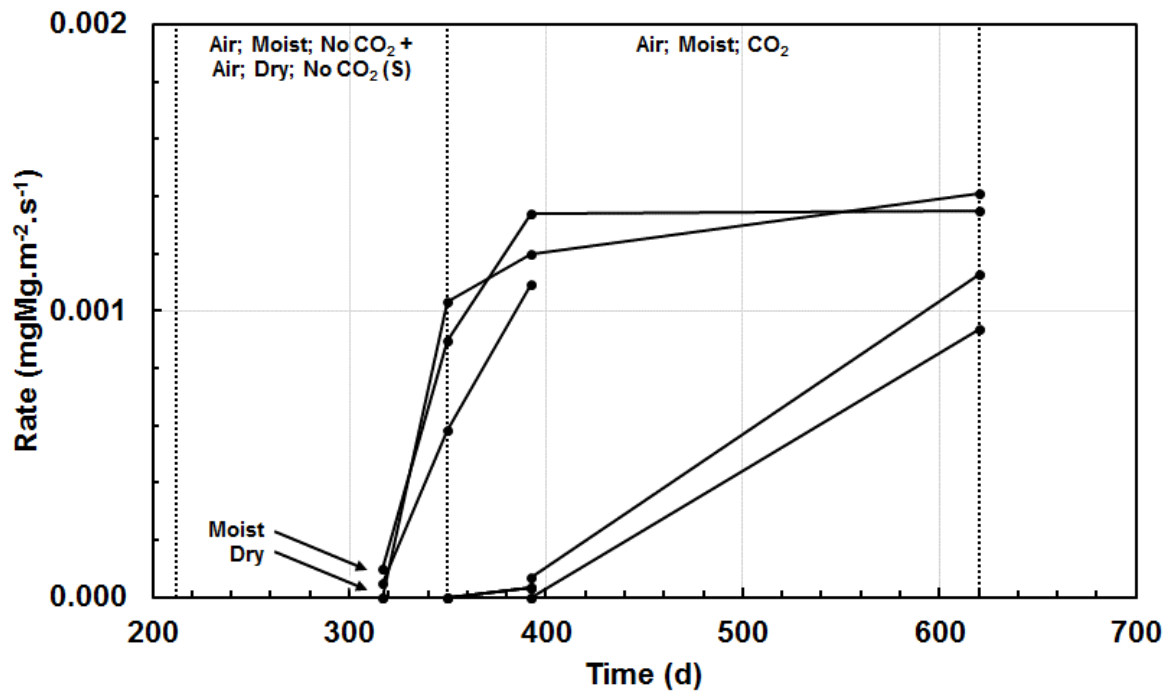
(b)

Figure 3. Measured corrosion rates for multiple individual Magnox ZR55 specimens under exposure conditions indicated, highlighting trends and variability. Please note that different x and y scale ranges are used in (a) and (b).
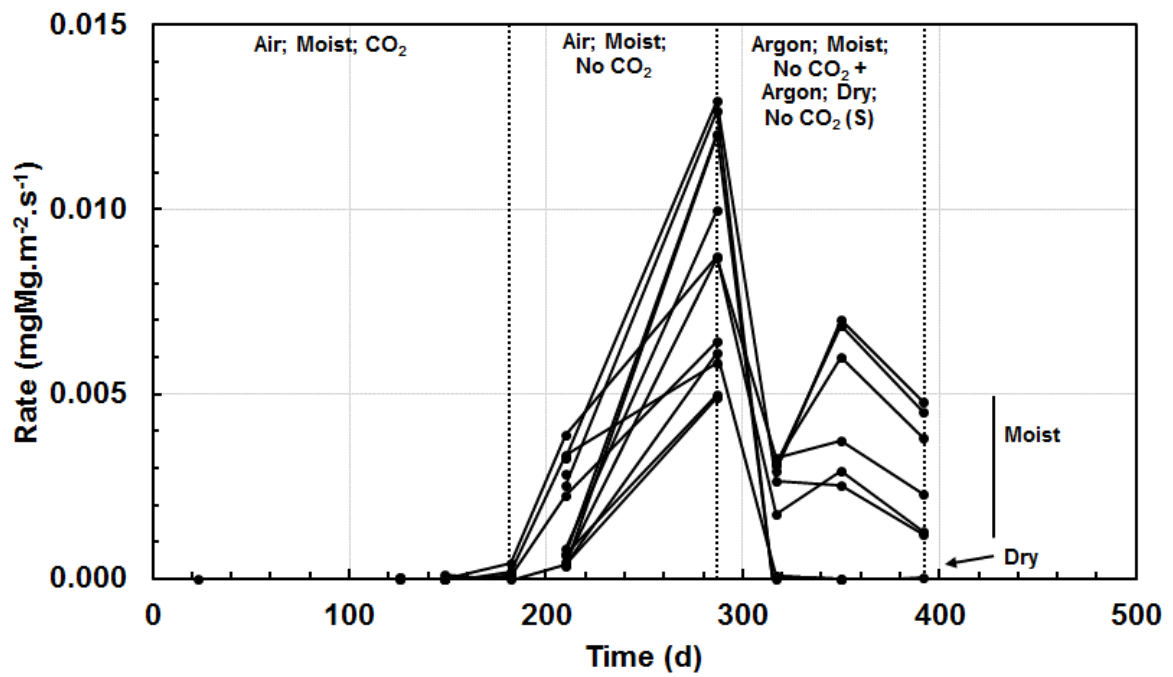
(a)
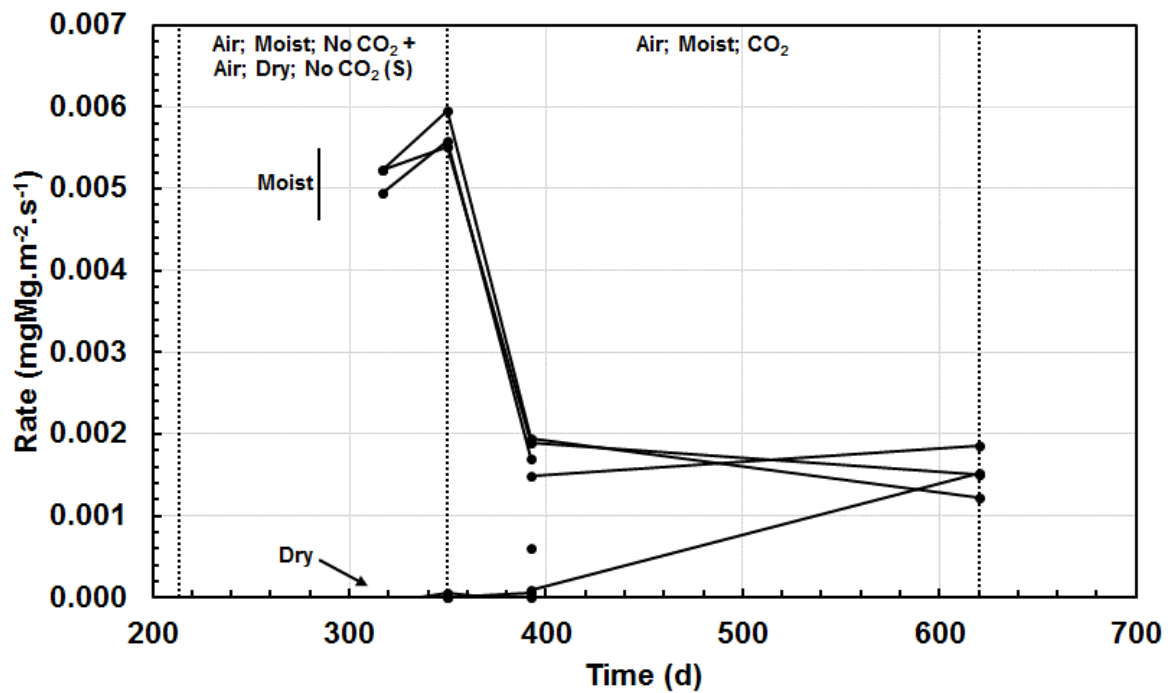
(b)

Figure 4. Measured corrosion rates for multiple individual pure magnesium specimens under exposure conditions indicated, highlighting trends and variability. Please note that different x and y scale ranges are used in (a) and (b).
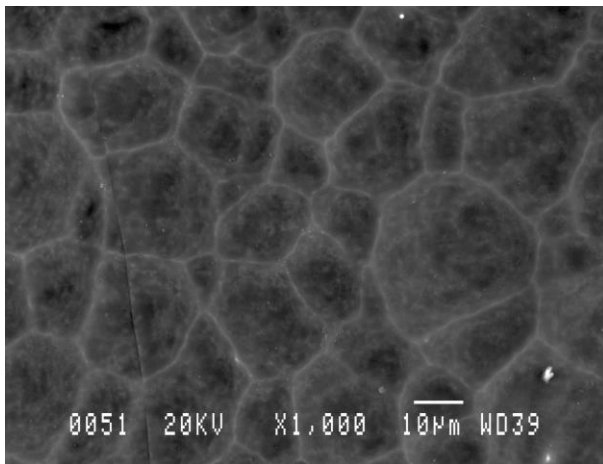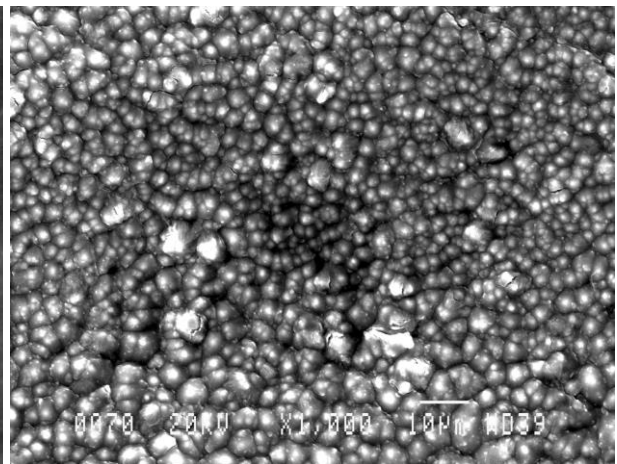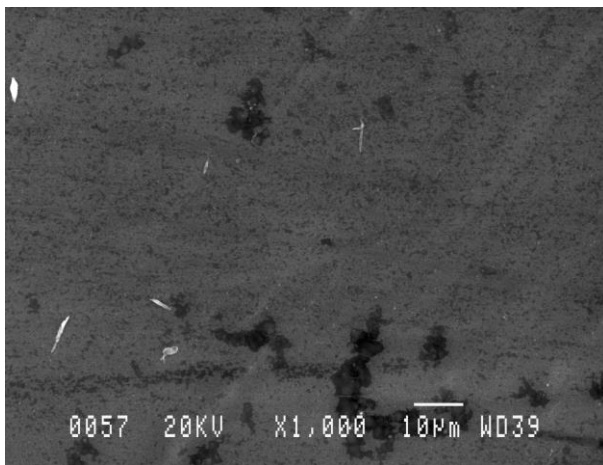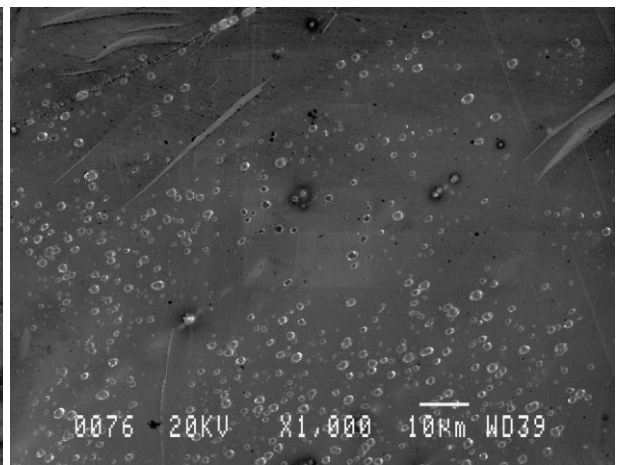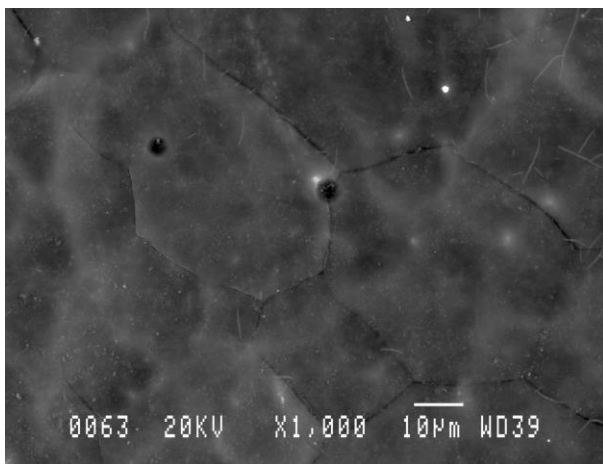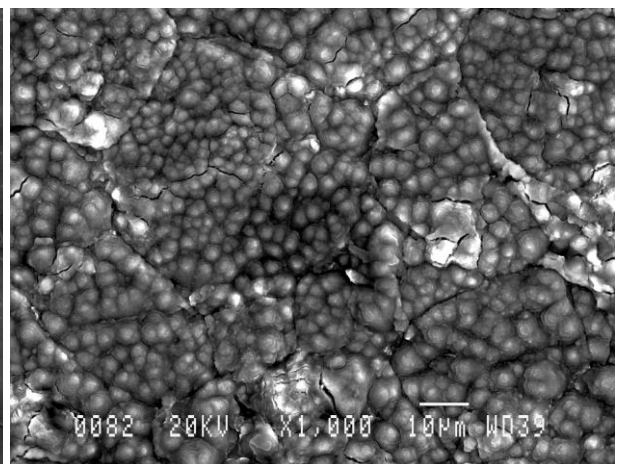
Figure 5. Scanning electron micrographs of: (a) Magnox AL80, laboratory air exposed; (b) Magnox AL80, four weeks' exposure to flowing moist air and no CO_2; (c) Magnox ZR55, laboratory air exposed; (d) Magnox ZR55, four weeks' exposure to flowing moist air and no CO_2; (e) pure magnesium, laboratory air exposed; (f) pure magnesium, four weeks' exposure to flowing moist air and no CO_2.
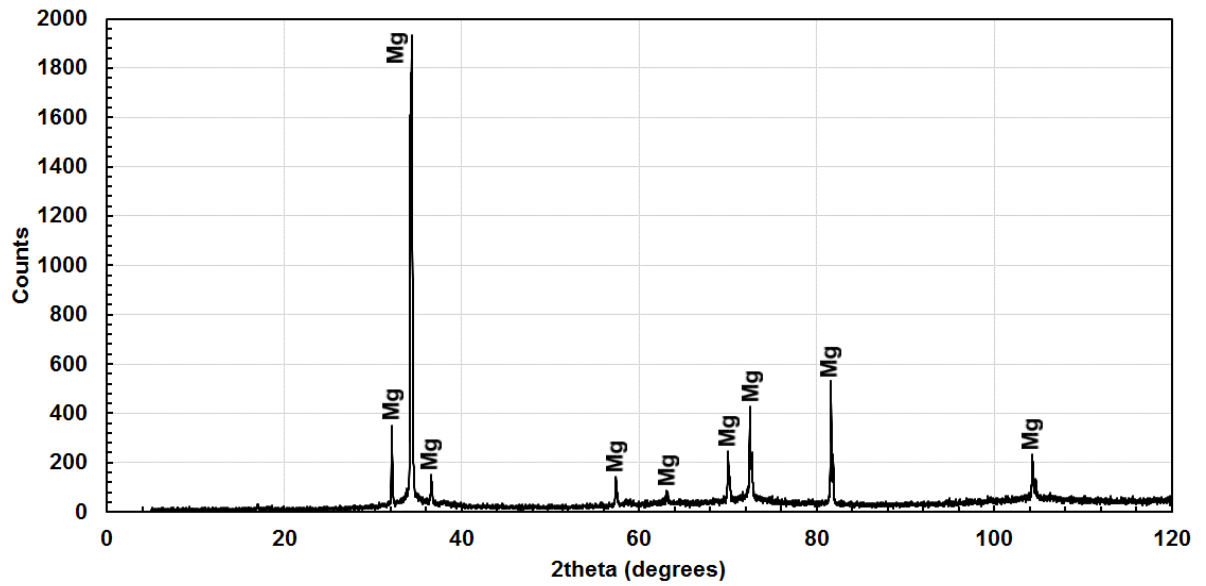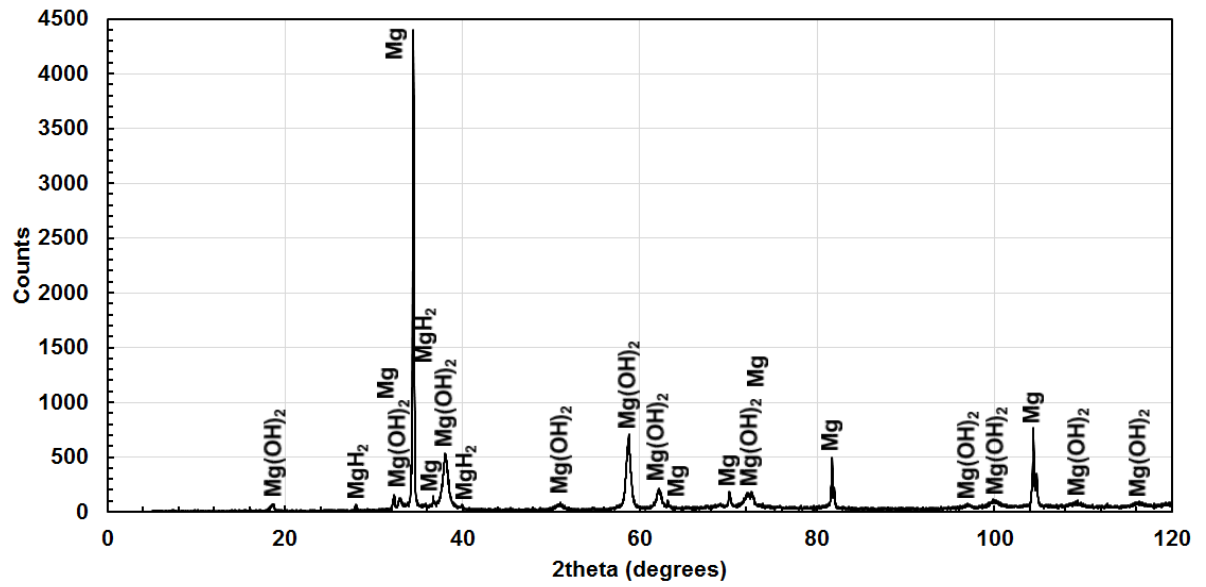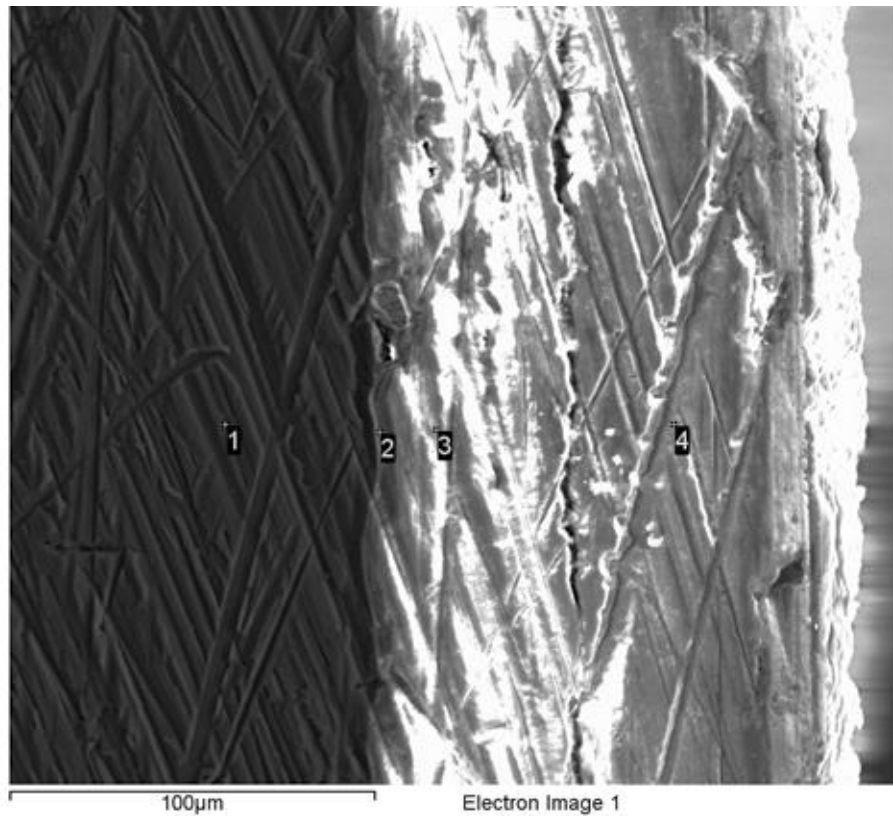
Figure 6. Phases identified via x-ray diffraction analysis (and reference to ICDD databases) on the surfaces of Magnox AL80 specimens after exposure to: (a) moist air, including CO_2; (b) moist air, no CO_2.

Position	Elemental composition (weight percentage)			
	Carbon	Oxygen	Magnesium	Aluminium
1	3.84	1.92	93.52	0.72
2	3.44	55.85	40.37	0.33
3	3.47	55.26	40.97	0.29
4	3.00	54.91	41.78	0.31

Figure 7. Scanning electron microscopy / energy dispersive x-ray microanalysis of mechanical cross-section (substrate to left; surface corrosion product to right) of Magnox AL80 removed after exposure to high humidity and no CO_2.
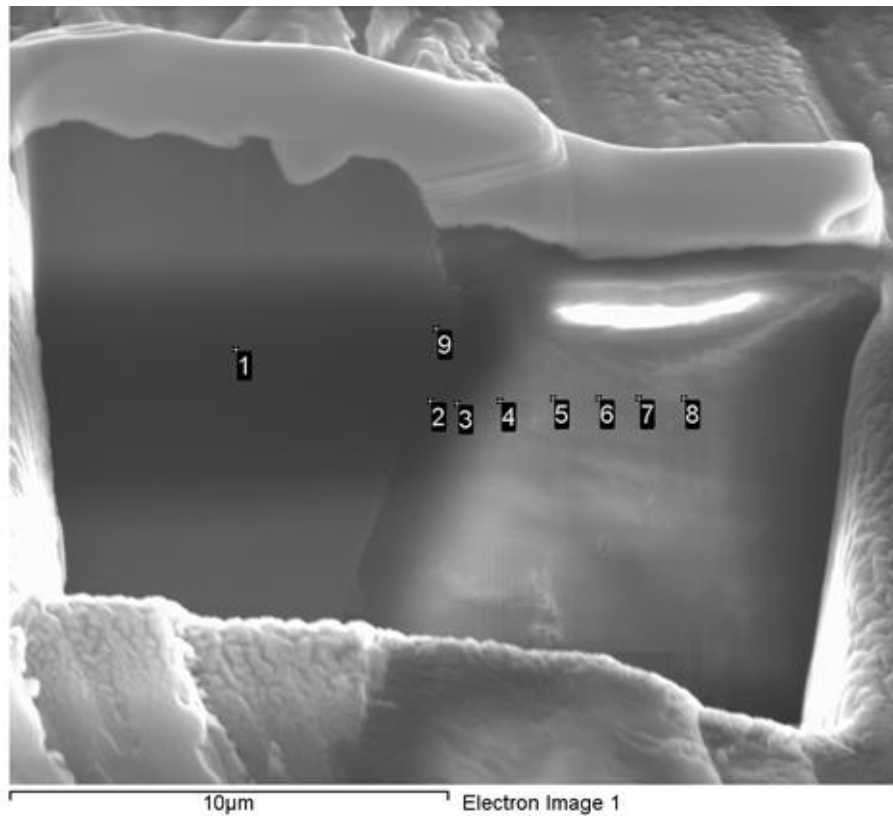
Position	Elemental composition (weight percentage)			
	Carbon	Oxygen	Magnesium	Aluminium
1	1.41	2.32	95.94	0.33
2	1.39	38.94	59.43	0.23
3	1.34	42.98	55.32	0.36
4	1.39	44.93	53.38	0.29
5	1.11	46.18	52.38	0.33
6	1.20	45.27	53.12	0.41
7	1.16	44.88	53.61	0.35
8	1.18	43.26	55.25	0.32
9	2.02	11.48	85.89	0.61

Figure 8. Scanning electron microscopy / energy dispersive x-ray microanalysis of ion beam cross-section (substrate to left; surface corrosion product to right) of Magnox AL80 removed after exposure to high humidity and no CO_2.
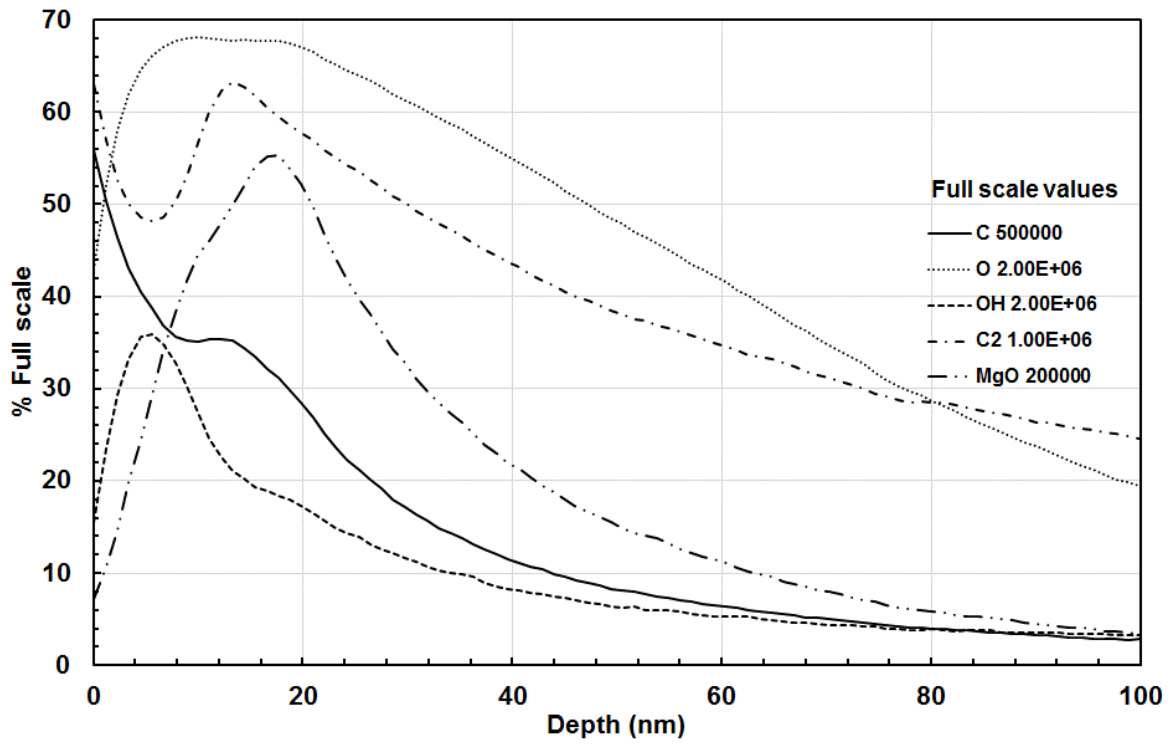
(a)
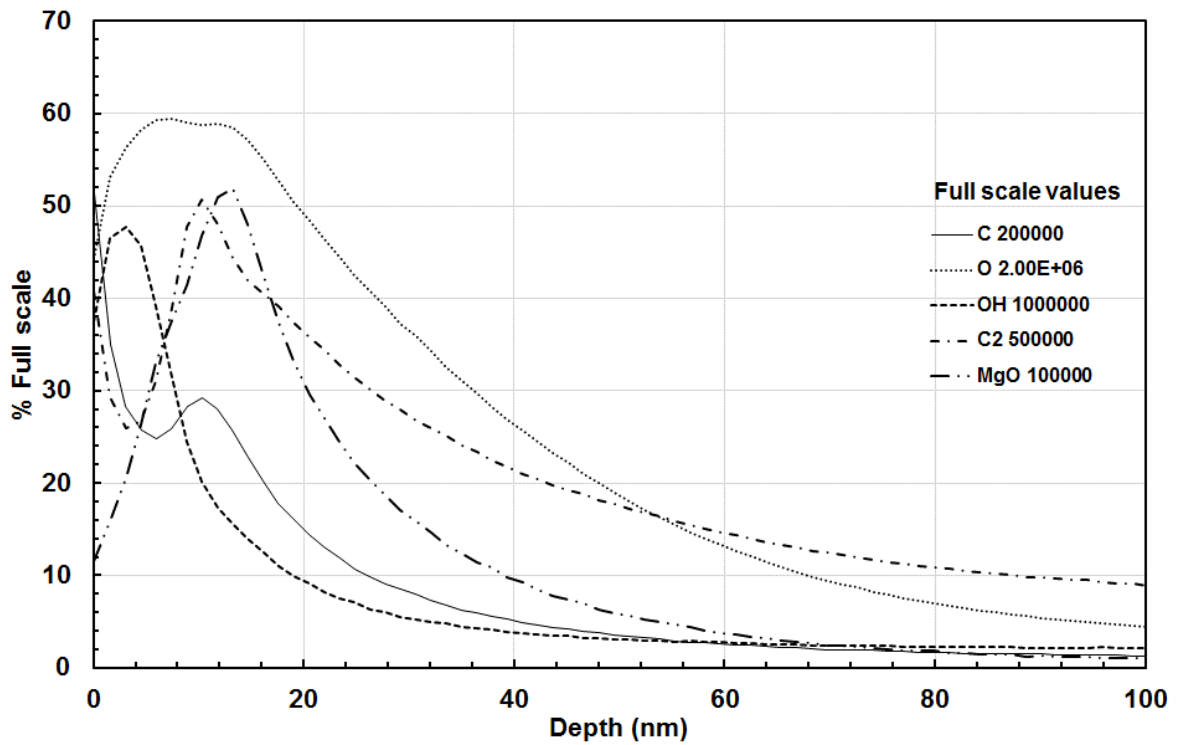
(b)

Figure 9. Negative secondary ion mass spectrometry depth profiles of Magnox AL80 following exposure to low relative humidity with CO_2 present in the gas stream (~90 °C vessel temperature; 182 days): (a) area 1; (b) area 2.
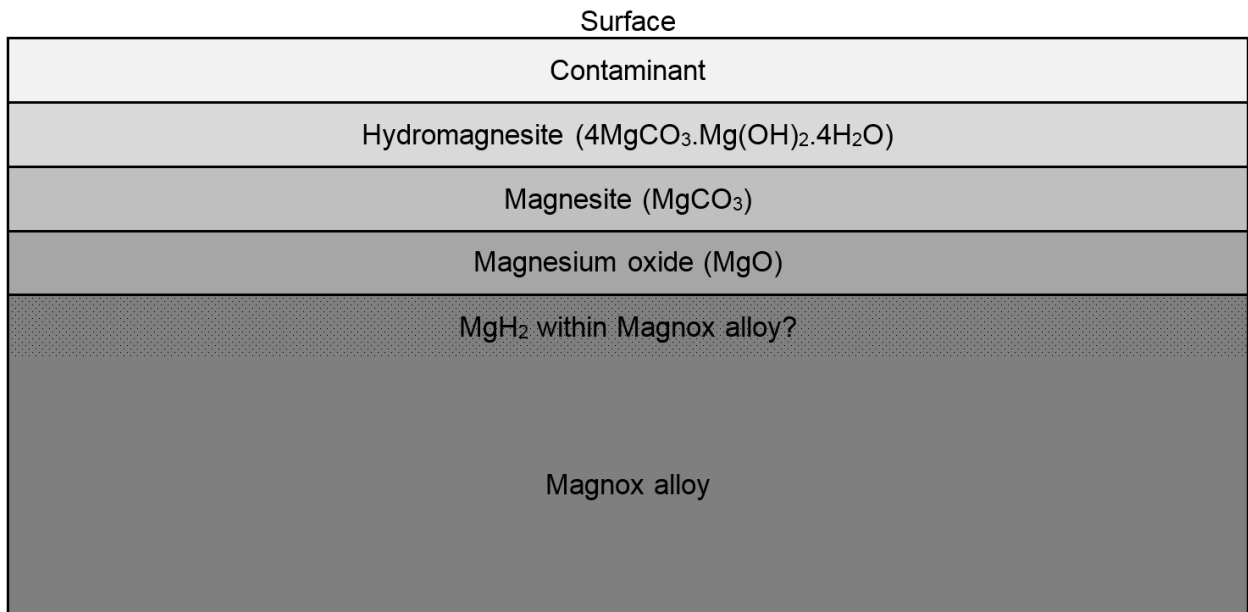
Figure 10. Schematic of proposed multi-layer corrosion product structure. It is likely that the MgH$_2$ is incorporated into the underlying metal. The relative thickness of each layer is not represented in this figure and each layer probably modulates in thickness.